2019-03-01

Characterization of Mechanical Properties of Thin-Film Li-Ion BatteryElectrodes from Laser Excitation and Measurements of Zero-Group Velocity Resonances

Jing Yao
Brigham Young University

BYU ScholarsArchive Citation

Yao, Jing, "Characterization of Mechanical Properties of Thin-Film Li-Ion BatteryElectrodes from Laser Excitation and Measurements of Zero-Group Velocity Resonances" (2019). *All Theses and Dissertations*. 7128.
https://scholarsarchive.byu.edu/etd/7128

Characterization of Mechanical Properties of Thin-Film Li-Ion Battery Electrodes from Laser Excitation and Measurements of Zero-Group Velocity Resonances

Jing Yao

A thesis submitted to the faculty of
Brigham Young University
in partial fulfillment of the requirements for the degree of

Master of Science

Brian A. Mazzeo, Chair
Greg Nordin
Dean Richard Wheeler

Department of Electrical and Computer Engineering

Brigham Young University

ABSTRACT

Characterization of Mechanical Properties of Thin-Film Li-Ion Battery Electrodes from Laser Excitation and Measurements of Zero-Group Velocity Resonances

Jing Yao
Department of Electrical and Computer Engineering, BYU
Master of Science

The mechanical properties of thin-film Li-ion battery electrodes are controlled by the micro structure of the constituent materials. In this work, a non-contact and non-destructive measurement of the mechanical properties of electrode films is performed by measurement of zero-group velocity (ZGV) resonances. The ZGV Lamb wave modes of a solid bilayer consisting of a thin metallic layer and a thin compliant coating layer are shown to be dependent on the Young's moduli, thicknesses, densities and Poisson ratios of the layers. Theoretical models are used to quantify the sensitivity of the ZGV resonances to changes in mechanical properties. Experimental ZGV resonances are excited using a pulsed infrared laser and detected using a laser interferometer. Commercial-grade battery films with different coating materials, densities and thicknesses are measured. Young's moduli of the battery electrode layers are estimated using the combination of a theoretical model and experimental results. The effect of the calendering process on the battery materials is also investigated. Results suggest that the Young's modulus of the electrode coating increases drastically after the battery films are calendered. This technique can be used to quantitatively study the mechanical properties of Li-ion battery electrodes to improve overall battery performance.

Keywords: Battery, Lamb waves, ZGV Lamb modes, Laser ultrasonic measurements, Material characterization

ACKNOWLEDGMENTS

I am very grateful for all of the support and encouragement from my wife, for believing in me when I am questioning myself. Her love and care helped me to get through this master's program. I also want to thank my family, for their love, care and help when I needed them. They have been very supportive and I am so grateful for them.

I would like to thank my advisor Dr. Brian Mazzeo for all of his help and guidance during the research project. He gave me the chance to work on a project requiring a broad background of knowledge, which led to a great learning experience. He also encouraged me and had faith in me even when I doubted myself. He is a true mentor who guided me to think like an engineer and helped me develop critical thinking skills. I would like to thank Dr. Dean Wheeler and Dr. Greg Nordin for their support and help in this research project.

The writer acknowledges Dr. Daniel Smalley and Dr. Stephen Schultz for their assistance with the interferometer equipment.

I also want to thank my colleagues in Dr. Mazzeo's research groups for meaningful discussions. Thanks to Joseph Cassler for his assistance on this project.

TABLE OF CONTENTS

LIST OF TABLES

LIST OF FIGURES

CHAPTER 1. INTRODUCTION

Batteries are everywhere nowadays. They are commonly used for drones, computers, smart phones, wearable devices and many other portable electronics. They are also playing a critical role in electric vehicles [1] and clean energy applications. Lithium-ion (Li-ion) batteries have a huge portion in the battery market, because of their advantages in high energy density ($>$ 200 mAh/g), high charge and discharge rate and long lifespan and cycling performance ($>$ 1000 times) [2]. The battery market continues to grow at a fast rate. There are billions of rechargeable batteries produced each year just for the consumer electronics market alone [3] and the demand is still growing. The need for better battery performance (stability, lifespan, energy density and power density) is likewise high.

1.1 Problem Statement

High performance and low-cost Li-ion batteries are always preferred by the consumers, but manufacturing cost reductions and achieving better performance are still challenges faced by the industry as a whole. Improved quality control and non-destructive evaluation methods are needed to reduce the scrap rate during manufacturing in order to reduce the cost [4]. Understanding, measuring and controlling the heterogeneity in battery electrodes is important to improve the performance of battery films such as high energy density, high power density and high durability [5], [6]. If problems with the battery electrodes are not identified during the manufacturing process, not only will it cause a decrease in the efficiency and performance of the battery, but also it increases the risk of safety hazards.

Local mechanical properties such as Young's modulus, density and thickness of the coating layer can be a good indication of heterogeneity in the battery films. They are important properties to measure before the battery films are integrated into a full cell. Because materials and processes change periodically during manufacturing, they also are indicators of changing fabrication conditions. Surface roughness and features with a small curvature can increase the risk of mechanical failure from high stress, decrease the power density and long-term durability of batteries [6]. Varying stiffness and thickness of the coating layer can also cause delamination and poor contact when battery films are stacked and rolled into a cell, a common packaging configuration [7].

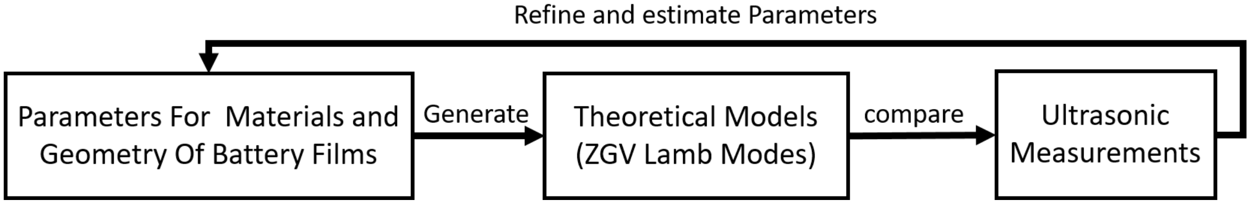

Figure 1.1: Diagram of the estimation approach used in this research.

In this research, I investigate ultrasonic measurement as a non-destructive and non-contact method to characterize the mechanical properties of Li-ion battery films. In particular, I investigated laser induced zero-group-velocity (ZGV) Lamb modes of Li-ion battery films. I report experimental results and theoretical results associated with the ZGV modes of a solid bilayer consisting of a thin metallic layer (aluminum or copper) and a thin coating layer. ZGV resonance frequencies of such a bilayer structure depend on materials' density, thickness, and elasticity of each layer. So a difference in these parameters causes different ZGV resonance frequencies. The results indicate that this method can be used to distinguish among films with different mechanical properties. Theoretical models have been created using GUIGUW 2.2 software developed by Bocchini *et al*. [8]. With known mechanical properties of the battery film materials, I simulated with the theoretical model a wide range of unknown parameters with wide intervals. Then I fitted the experimental results to the theoretical model to find a more accurate range of the unknown parameters. This procedure was repeated until the desired resolution of the unknown parameters was reached. This approach can be summarized in Fig. 1.1. Additionally, the effect of the mechanical properties of battery films due to the calendering process is investigated. The experimental results shows that the elasticity of the battery coating increases drastically due to calendering.

The long-term goal of this research is to develop an acoustic probe to detect small variations in a battery film's local material properties such as density, thickness and elasticity. This proposed probe can be used as an aid to a conductivity probe developed at BYU [9] to better understand the

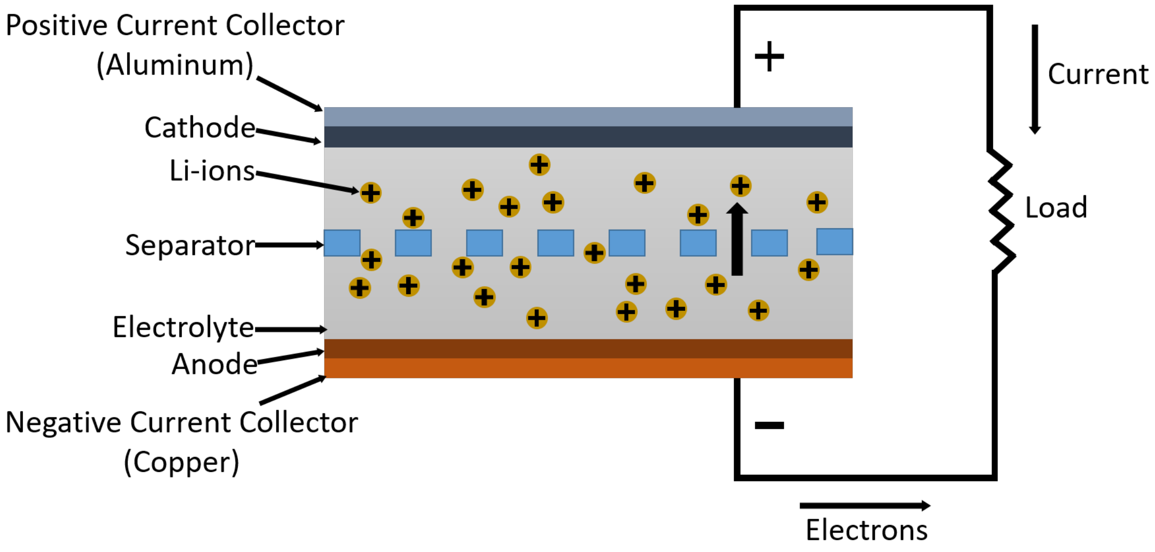

Figure 1.2: Diagram of a battery cell when discharging. The Li-ions move from anode to another cathode through separator to create electrons flow between the current collectors through the load.

battery electrode properties. This combination of measurements can provide useful information for modeling work and process improvement.

1.2 Background Knowledge of Li-ion Batteries

1.2.1 How Li-ion Battery Works

A typical Li-ion battery cell generally consists of an anode, cathode, separator, electrolyte, and positive current collectors and negative current collectors. A diagram of a battery cell is shown in Fig. 1.2. The anode and cathode are used store the lithium. The separator blocks electrons and passes ions. The electrolyte is a solution that carries positively charged lithium ions from the anode to the cathode when discharging. When discharging, lithium ions move through the separator and create free electrons in the anode which generates a charge at the positive current collector. This movement promotes the current flow through the load (computer, phone, etc.) to the negative current collector as shown in Fig. 1.2. When charging, the opposite happens, Li-ions are released by cathode and received by anode [7]. The cells can be connected in parallel or series to provide for different needs with battery casing. When cells are connected in parallel, it provides higher charge capacity (Ah) while maintaining the same voltage for each cell. By connecting battery cells in series, it can provide higher voltage while maintaining the capacity (Ah).

Energy density and power density of batteries are the two common concepts used to determine the battery performance. Energy density (Wh/kg) is the amount of energy that can be stored in the battery with respect to its mass. Power density (W/kg) shows the power that can be generated by the battery with respect to its mass. Both of these parameters are very important to consider for different applications. For examples, batteries used for cell phones should provide a low but stable power for a long time, which means high energy density and low power density. But the batteries for a hybrid car requires high power density to initiate the car movement; on the contrary, the energy density does not need to be high since those batteries will be charged while driving.

1.2.2 Battery Film Structure

Li-ion battery electrodes generally consist of a thin, metal current collector coated with anode or cathode material on both sides. In most battery manufacturing processes, the battery coating materials first are mixed as a wet slurry, then the slurry is applied to the metal current collector. After the electrodes are dried, they are calendered to a specific thickness. The calendering process increases the density and compresses the pores of the electrode. The electrode films are layered with separators and rolled into a battery cell package. At last, the electrolyte solution is added to the cell [7].

An example of a cathode (single-sided) before the calendering process is shown in Fig. 1.3. The battery film is a bi-layer structure, consisting of a current collector layer and a battery coating layer. The current collector layer is commonly made of thin aluminum for cathode or copper for anodes. On top of the current collector is the coating layer composed of large active material particles, carbon additive for better conductivity, polymeric binder, and pores [10]. The distribution of this mixture of materials can vary significantly in structure due to manufacturing differences, thus causing the heterogeneity on the micron as well as on the millimeter-scale [9], [11].

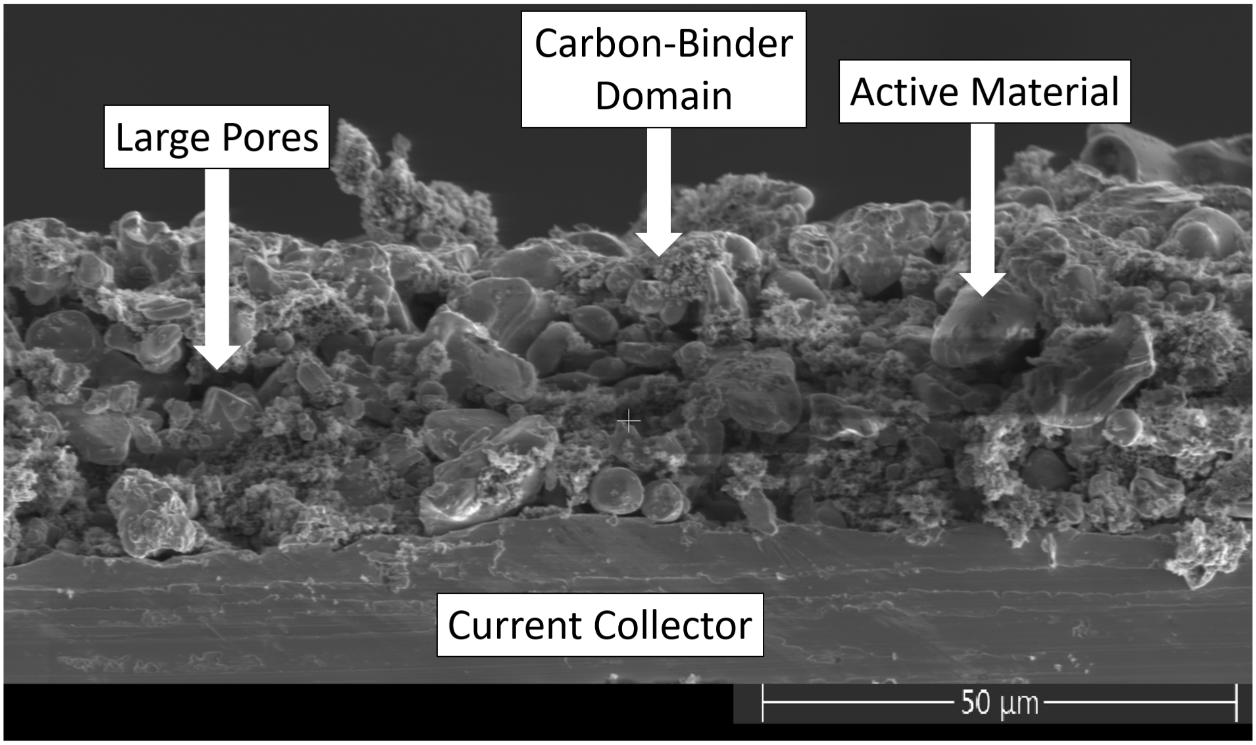

Figure 1.3: Scanning electron microscope micrograph of the cross section of an uncalendered Li-ion cathode battery film. The bottom layer is the aluminum current collector. The top layer is the cathode coating and is made up of three distinct phases: an active material lithium cobalt oxide (LCO), carbon conductivity additive and polymeric binder (nanoporous gray filler between the active material), and pores (dark spaces between the active material and binder).

1.3 Impact

Being able to measure the heterogeneity of battery electrodes and to correlate it with the performance of batteries is an important challenge faced by the researchers and manufacturers as a whole. This work uses mechanical properties to correlate with heterogeneity problems of battery electrodes. Several techniques have been previously used to measure the mechanical characteristics of thin film, such as nanoindention [12], Brillouin scattering [13], and laser ultrasonic methods [14]–[16]. Many of these techniques used in the industry are destructive in some way. For examples, small pieces of samples are normally cut from original films to perform thickness measurements and density evaluations. For Young's modulus estimations of a battery coating layer, many techniques require the coating layer to be delaminated from the current collectors.

This work extends a laser ultrasonic technique to measure and characterize the mechanical properties of battery electrodes. This method is developed with a goal of non-contact, non-destructive and accurate measurement and providing information of battery electrodes specifically for the battery researchers. This work makes that goal possible. The results indicate that this method can be used to distinguish among films with different mechanical properties. Additionally, the effect of the mechanical properties of battery films due to the calendering process is investigated. Since the method is non-destructive, it can potentially be used to reduce the scrap rate during the quality control process to reduce the manufacturing cost. While this work has been primarily motivated by Li-ion batteries, this work can be generalized to measure ZGV Lamb wave modes of a thin compliant layer on a thin metallic layer structure.

1.4 Background of Acoustic Measurements

Acoustic methods have been extensively used for measuring the mechanical properties of materials in materials and structures. Acoustic measurement techniques are commonly found in concrete evaluation, non-destructively finding defects in ships and aircrafts structures and testing the coating used in industrial processes for protecting surfaces from environments [17].

A common method of measuring thin films or membranes is using the acoustic resonances of a circularly clamped area. The resonance can be excited by a pulsed laser or a wide frequency range of sound burst, and can be measured using a laser interferometer or a speaker. This method can estimate the Young's modulus and thickness [10]. But due to uneven clamping resulting in variations of the boundary conditions, the method has exhibited greater systematic variation than would be ideal for monitoring changes in battery properties [10].

Guided wave propagation has often been employed to investigate the mechanical properties or defects in one-layer or multi-layer structures through Lamb waves [14], [15], [18]. Lamb waves are guided waves in thin plates. Lamb waves are dispersive, which means their phase velocities, v_p, of propagation depend on the angular frequency (ω) (or wavelength (λ)), which are dependent on the elastic constants, densities, and thickness of the layer.

For some Lamb wave modes, the group velocity goes to nearly zero at finite wavelength [19], which exhibits the extraordinary phenomenon of a spatially local resonance with certain frequencies determined by the material properties and the physical arrangement of the materials, because the energy does not propagate away from the excitation region when group velocity goes to zero. These modes are known as zero group velocity (ZGV) modes. Due to the localized resonances, ZGV modes are ideal for localized measurements of material properties because the clamping of the material is not important if excitation and measurement are sufficiently far from the clamping boundaries. ZGV modes have been used for locally measuring the Young's modulus or thickness of single-or multi-layered materials [17], [20], [21]. ZGV modes can be generated by a impulse from a pulsed laser source and detected using a laser interferometer [20]. The deposited energy by the pulsed laser source is absorbed and transformed into mechanical waves through the thermal-elastic effect [22]. The amplitude of ZGV resonances depends on the deposited energy, the shape of the pulse laser beam [23], and the thermal-elasticity of the interrogated material. The numerical study of plates with continuous material variation across the thickness by Tofeldt *et al*. [24] points out that the lowest ZGV modes of such a structure can have similar behavior and detectability as single isotropic layer structure.

SAWs mainly propagate along the surface of a material. They can be generated using high frequency transducers, laser impulses or continuous laser beam and can be measured using another high speed transducers or laser interferometers. Since the SAWs penetration depth is proportional to the wavelength of the wave which is determined by the frequency of the wave, it can be used for measuring materials in a multi-layer structure. At different frequencies, the wave interacts with different layers in the structure, causing a dispersion relationship to the wave velocity. The dispersion relations are used to find the elasticity and thickness of the thin film [25]. The SAWs method has been used in finding the mechanical properties such as thickness and Young's modulus of films from 40 nm to 1 µm thick [18], [26]–[28]. It has also been used in finding the temperature effect on Young's modulus of alloys [29] and measuring damage of a steel surface [30]. The results from SAWs measurement is very similar or even better than the results from nanoindention method [31], [32].

While many of the acoustic methods discussed above can be good candidates for measuring thin-film battery electrodes, we extend the laser measurements of ZGV Lamb modes method to measure the mechanical properties of battery electrodes. The laser excitation can avoid physical contact with battery films, and the ZGV Lamb modes can be a good indicator of the mechanical properties of local regions. Additionally, it is a relatively faster measurement than other acoustic methods because it only requires the measurement of one Lamb wave mode generated by a pulsed laser while other methods like SAWs method need to generate and measure different modes to form dispersion curves in order to extract the mechanical properties of target materials.

1.5 Thesis Structure

This thesis is organized in the following order. In Chapter 2, an overview of the theory of Lamb wave in a bilayer structure is shown, and simulations are used to how ZGV Lamb modes respond to show the change of coating mechanical properties. Chapter 3 describes the experimental setup, the testing procedures, and the processing method for the acquired data. Chapter 4 shows the experimental results which are discussed in Chapter 5. Chapter 6 gives a summary, suggestions for future work and a conclusion.

CHAPTER 2. THEORY

2.1 Lamb Waves in Bi-Layer Structure

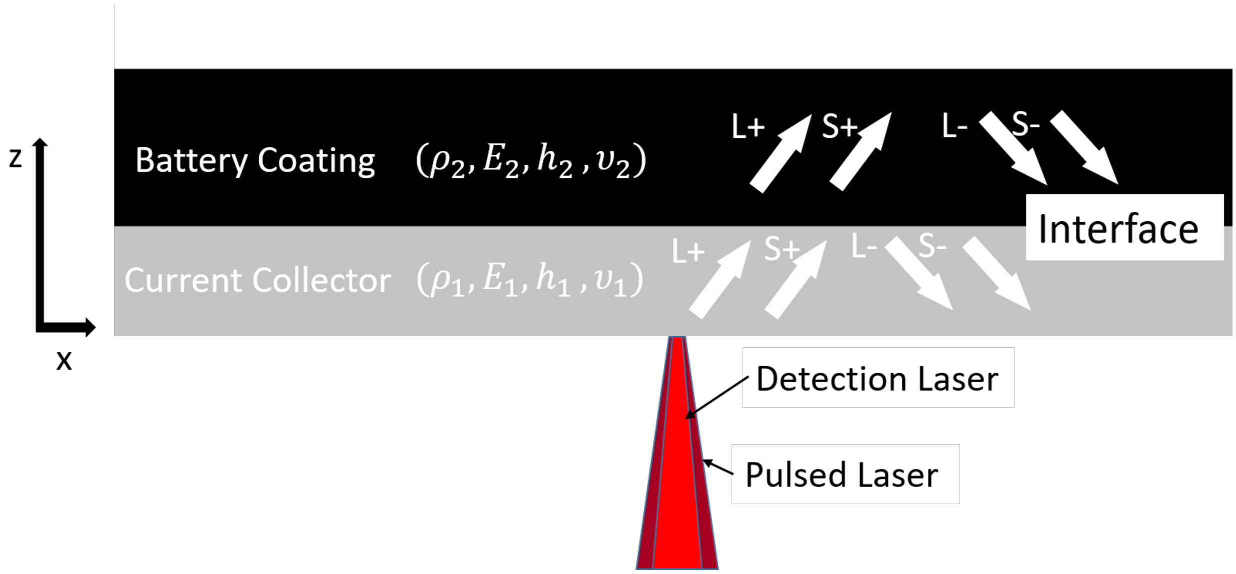

Figure 2.1: Diagram of excitation and detection of Lamb waves in battery films using laser excitation and measurement. The bilayer structure represents the structure of electrode films (a thin coating layer on a thin metal current collector). A laser pulse generates Lamb waves in the materials and a detection laser probes surface displacement.

Lamb waves are elastic waves that propagate in solid plates. A single-sided battery film is a solid bilayer structure consisting of a metal current collector layer and a battery coating layer as shown in Fig. 2.1. The current collector materials are generally uniform and consist of a single metal layer, for example, a 20-μm-thick aluminum sheet for cathodes, or a 10-μm-thick copper sheet for anodes. In a high quality battery film, the current collector and battery coating are assumed to be rigidly held together. The region of interest, interrogated by the mechanical waves excited by the laser pulse, consists of a few cubic microns. In that small region, the materials are assumed to be homogeneous, isotropic, and elastic. This assumption allows us to evaluate different regions because it is known that the battery coating is heterogeneous, and the material properties change from point to point [9]. The layers above and below the film are considered as vacuum because the difference of acoustic impedance between air and the materials is very high. In Fig. 2.1, ρ_i, E_i, ν_i, h_i represent the density, Young's modulus, Poisson ratio, and thickness, respectively of each layer denoted by i. Layer 1 is the current collector and layer 2 is the battery coating.

When the laser pulse illuminates the surface of the small target region of the current collector, the majority of the energy will be scattered and reflected, but deposited energy will be absorbed and produce mechanical waves because the thermal-elastic effect causes stress difference along the surface. Such an impulse excitation induces a broadband set of Lamb wave modes [20], [33]. These mechanical waves can be more easily understood using acoustic bulk waves: longitudinal waves and shear waves. These waves propagate through the materials and are reflected at the material interface and the free surfaces as illustrated in Fig. 2.1. L and S represent longitudinal and shear waves, respectively, and positive and negative sign denote the vertical propagation direction. The velocities of longitudinal wave and shear wave are shown in Eqs. 2.1 and 2.2 [34], where

$$V_l = \sqrt{\frac{E(1-\nu)}{\rho(1+\nu)(1-2\nu)}} \tag{2.1}$$

$$V_s = \sqrt{\frac{E}{2\rho(1+\nu)}}. \tag{2.2}$$

The acoustic bulk wave velocities are dependent on E, ρ, and ν through these equations. From these equations, it is clearly seen that the acoustic bulk wave velocities increase when E increases and the velocities decrease when ρ increases.

Lamb waves are dispersive, which means their phase velocity and group velocity depend on the angular frequency ($\omega = 2\pi f$, where f is frequency) as well as the elastic constants, densities, Poisson ratios and thicknesses of the constituent materials. When the parameters E, ρ, ν, and h are known for eac layer, a set of dispersion curves, (wavenumber, k, versus frequency, f) can be calculated for the Lamb waves in the bilayer structure. Unlike the analytical closed form solutions available for Lamb Waves in a single layer [35], [36], Lamb waves in a multi-layered structure do not have analytical closed forms, which makes Lamb wave analysis for bilayers more challenging.

2.2 Simulation and Analysis

Numerically solving for the dispersion curves have been very well studied. One way is to use a widely acknowledged method: the semi-analytical finite-element (SAFE) [37], [38] method. When the SAFE method is applied to our system, it assumes the guided waves propagate harmonically along the y direction (orthogonal to x and z direction) as shown in Fig. 2.1, meaning the displacement, stress and strain are the same along the x direction. This reduces the simulation complexity from 3-dimensions to 2-dimensions. The cross section is then discretized to approximate the solutions of the wave equations numerically [8], [38] using the finite element method.

The software GUIGUW 2.2 developed by Bocchini *et al*. [8] employing the SAFE method was used to simulate the dispersion curves for different battery films with varying layer thickness and mechanical properties.

For our simulations, the geometry in Fig. 2.1 is used and no material damping is taken into account. The simulation parameters are shown in Table 2.1. The current collector (aluminum) listed in that table is used for all the simulations in this section. The density and Young's modulus values of coating 1 and coating 2 are the measured and estimated values of battery electrode films from Dallon *et al*. [10] The Poisson ratio of coating 1 and 2 is assumed to be the common value [39]. V_l and V_s are the velocities of longitudinal wave and shear wave calculated from Eqs. 2.1 and 2.2, respectively. The thicknesses of the coatings are chosen to be the same for comparison purposes. From the simulation parameters, two cases for different battery films are simulated. Case C1 is the battery film consisting of coating 1. Case C2 is the battery film consisting of coating 2. Two reference cases of a single layer structure are also simulated for cases C1 and C2. Reference R1 is a single layer of coating 1, and reference R2 is a single layer of coating 2. Both reference cases are set to have same thickness ($h = 46$ μm) as the total thicknesses of C1 and C2. Reference cases R1 and R2 are simulated to show how the dispersion curves change when part of the coating changes to metal current collector.

In general, the density (ρ) and thickness (h) of the coating layer and current collector layer have the same order-of-magnitude. The Poisson ratios of these two layers are also close. In contrast, the E values for these two layers have more than one order-of-magnitude difference. Additionally, the E values of the coatings themselves also have one order-of-magnitude difference. These two cases can be considered representative of different battery film conditions.

Table 2.1: Mechanical parameters of battery film used in the numerical models. Aluminum and copper are commonly used for current collectors for cathodes and anodes, respectively.

Material	ρ (g/cm^3)	E (GPa)	h (μm)	ν	V_l (m/s)	V_s(m/s)
Aluminum	2.700 [40]	70 [40]	20	0.334 [41]	6244	3117
Copper	8.960 [42]	128 [42]	10	0.36 [42]	4900	2292
Coating 1	2.479	5.04	26	0.3	1661	888
Coating 2	3.055	0.344	26	0.3	389	208

The simulated dispersion curves for cases C1 and C2 are shown in Fig. 2.2a and 2.2b, respectively. Only the four lowest Lamb wave modes are shown in Fig. 2.2. These four modes are denoted M1, M2, M3, and M4. The dispersion curves for references R1 and R2 are also shown in Fig. 2.2a and 2.2b, respectively, for comparison (black dotted lines). The four lowest modes for both reference cases are commonly denoted as A0, S0, A1, and S1. A and S represent asymmetric modes and symmetric modes, respectively. M1-M4 modes exhibit a similar pattern to the pattern of the four lowest modes for their corresponding reference cases. It can be observed that both C1 and C2 have higher temporal frequency f at a given wavenumber k for each mode respectively compared to their reference cases. In general, it is suggested that each mode shifts to higher frequency at given wavenumber (k), when part of the material (R1 and R2) changes into another material (C1 and C2) with higher acoustic velocities (V_l and V_s). The M1-M4 modes can not be represented using asymmetric and symmetric modes because there is no longer symmetry in Lamb waves propagation due to the wave interaction between the two different layers in C1 and C2.

In Fig. 2.2, the arrows denote ZGV points where the group velocity ($v_g = d\omega/dk$) [43] of the waves becomes zero. The ZGV modes exist only where v_g changes from negative to positive on the dispersion curve [20]. Negative and positive sign of v_g represent the propagation direction of the group velocity of Lamb waves. Because the group velocity is zero, the energy confined in those modes will not propagate away from the source point which is called the ZGV point. The corresponding non-zero wavenumbers (k) indicate that these ZGV modes have finite wavelengths given by $\lambda = 2\pi/k$. At the ZGV point, local resonances at ZGV frequencies occur after proper excitation. Detected ZGV resonances will show up as sharp peaks in the spectra of measured vibrations [20]. Thus, ZGV Lamb modes can be good indicators of the local mechanical properties

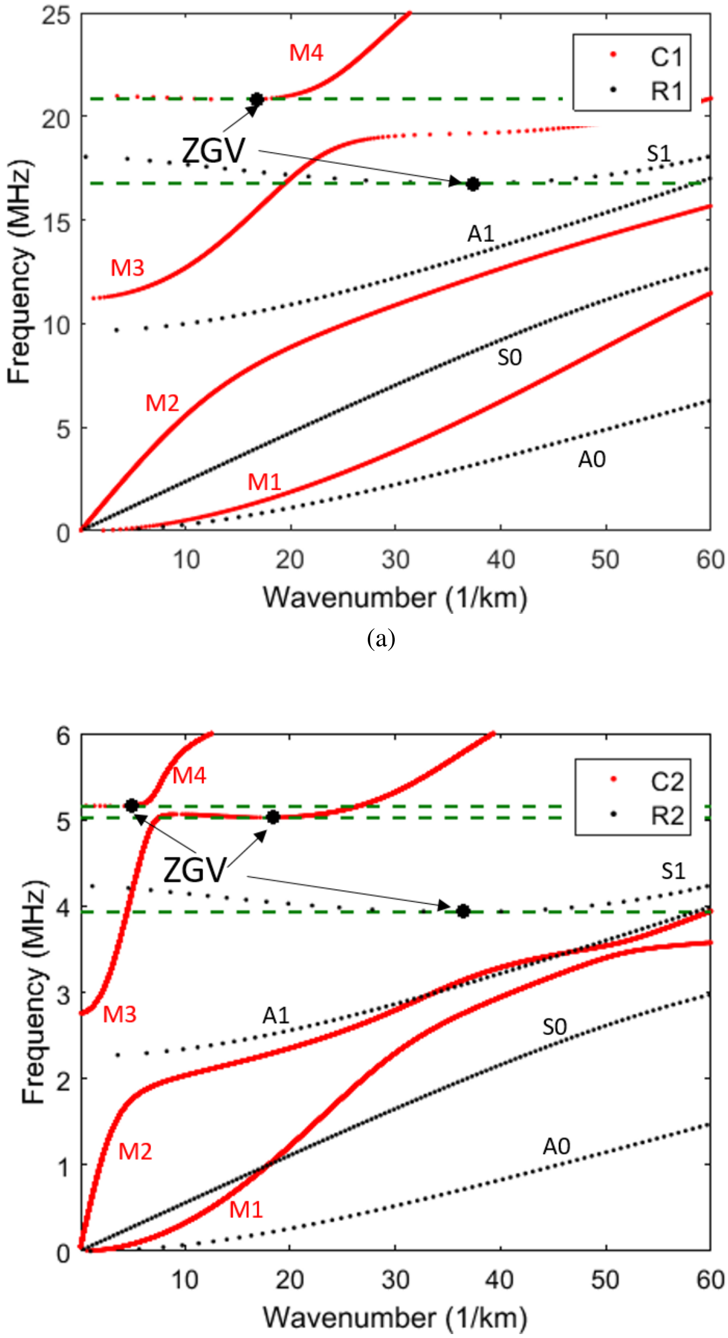

(a)

(b)

Figure 2.2: Dispersion curves simulated using the parameters from Table 2.1 and the simulation geometry in Fig. 2.1. (a) C1: coating 1 on aluminum. (b) C2: coating 2 on aluminum.

of locally excited regions. Due to their non-traveling property, the detection point should be close or coincident with the excitation point, as illustrated in Fig. 2.1.

As shown in Fig. 2.2a, case C1 has only one ZGV mode denoted as M4-ZGV. As shown in Fig 2.2b, case C2 has two ZGV modes denoted as M3-ZGV and M4-ZGV. The corresponding ZGV modes in reference R1 and R2 are denoted as the S1-ZGV mode. Higher other ZGV modes can also exist in dispersion curves for both cases. Even though several ZGV modes can exist, some ZGV modes are easier to excite than others using laser impulse excitation which is essentially broadband excitation of all frequencies. In general, the lowest ZGV modes can be more easily excited and detected at the ZGV point [24]. Both M4-ZGV mode and S1-ZGV mode are the 4th mode for each case , and both modes exhibit a similar pattern as shown in Fig. 2.2a and 2.2b. From the simulations of Tofeldt *et al*. [24], the M4-ZGV mode of a plate with continuous material variation across the thickness has similar behavior and detectability as the S1-ZGV mode of a single isotropic layer structure. We extend those results to our structures by considering the film structure as an extreme case of their study. In Case C1 the lowest ZGV mode is the M4-ZGV mode and this appears reasonable. However, in Case C2, two ZGV modes M3-ZGV and M4-ZGV exist and are closely related in frequency.

The displacement mode shapes of the M3-ZGV and M4-ZGV modes as a function of the plate thickness coordinate z for cases C1 and C2 are shown in Figs. 2.3 and 2.4, respectively. The profiles of the vertical displacement mode shapes for case C1 and C2 are shown in Fig. 2.3a and 2.4a, respectively. Similarly, the horizontal displacement mode shapes for case C1 and C2 are shown in Fig. 2.3b and 2.4b, respectively. The corresponding displacements of the S1-ZGV mode for references R1 and R2 are also shown. The horizontal dashed line represents the interface between the battery coating layer and current collector layer. The amplitude of the profiles is normalized to the same maximum magnitude of displacement for all the profiles. It is seen that the displacements of the battery coating layer are higher than the current collector layer in both vertical and horizontal directions for both cases. This is because the battery coating layer is a relatively ”soft” material compared to the current collector layer, so the ”soft” material tends to have higher displacements than the ”hard” material for a given mode.

Fig. 2.3 shows that M4-ZGV mode of case C1 can be treated as a distorted mode of the S1-ZGV mode of reference 1 when part of the coating material properties changes into a material that

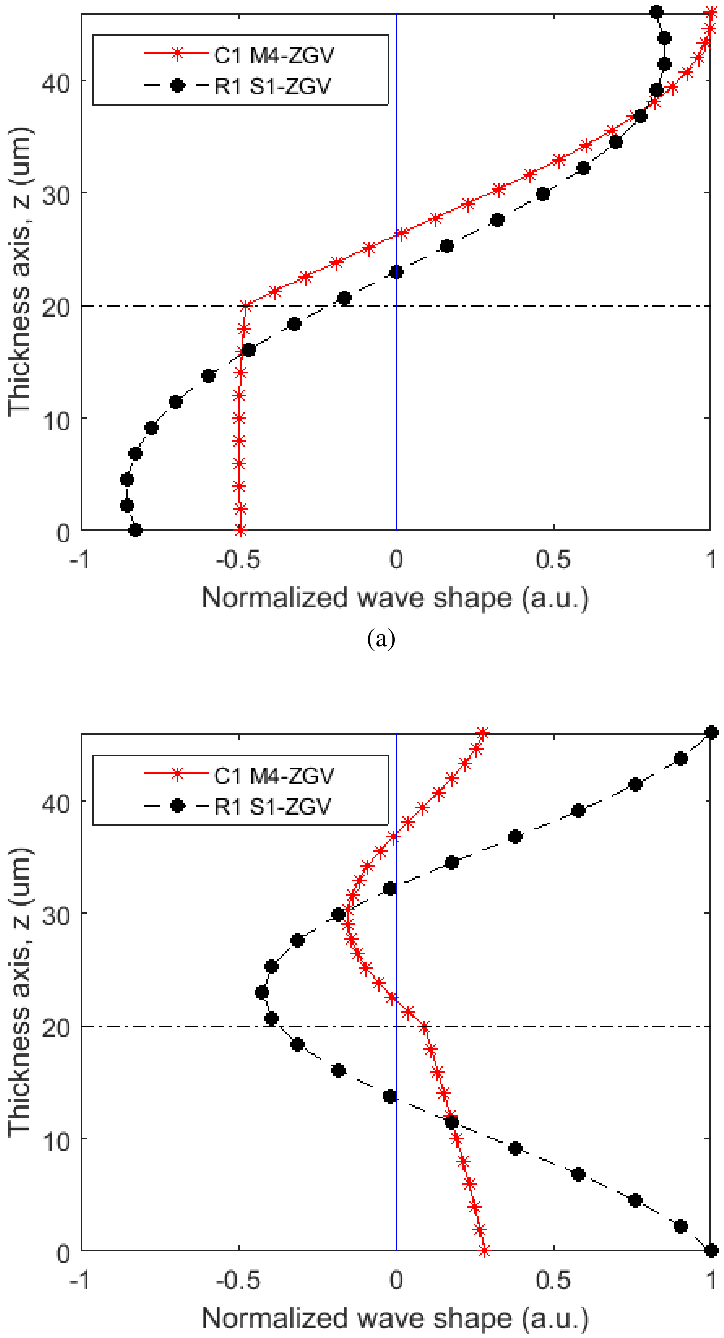

(a)

(b)

Figure 2.3: Profiles of displacement mode shapes (a) in the vertical direction and (b) in the horizontal direction for case C1 and reference R1.

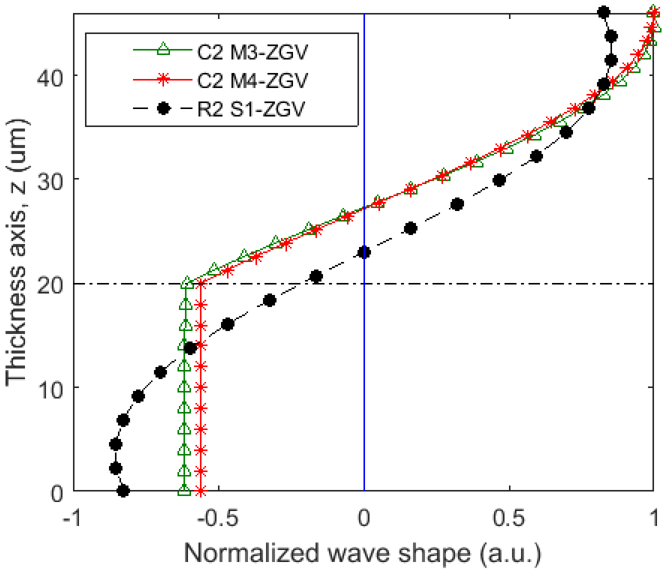

(a)

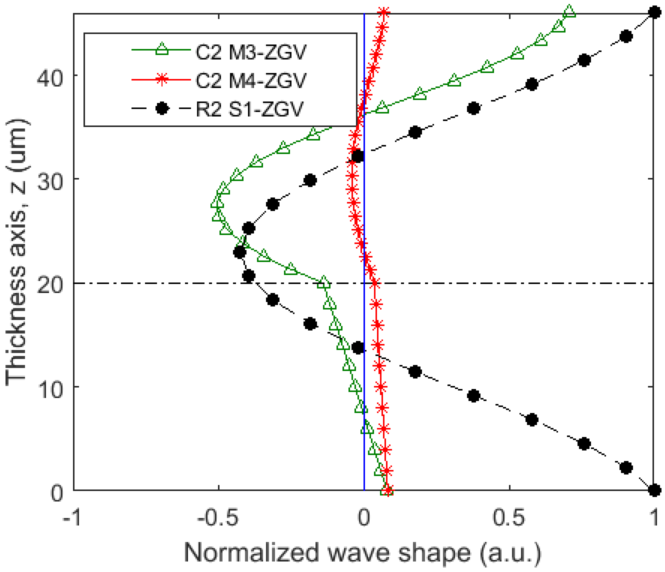

(b)

Figure 2.4: Profiles of displacement mode shapes (a) in the vertical direction and (b) in the horizontal direction for case C2 and reference R2.

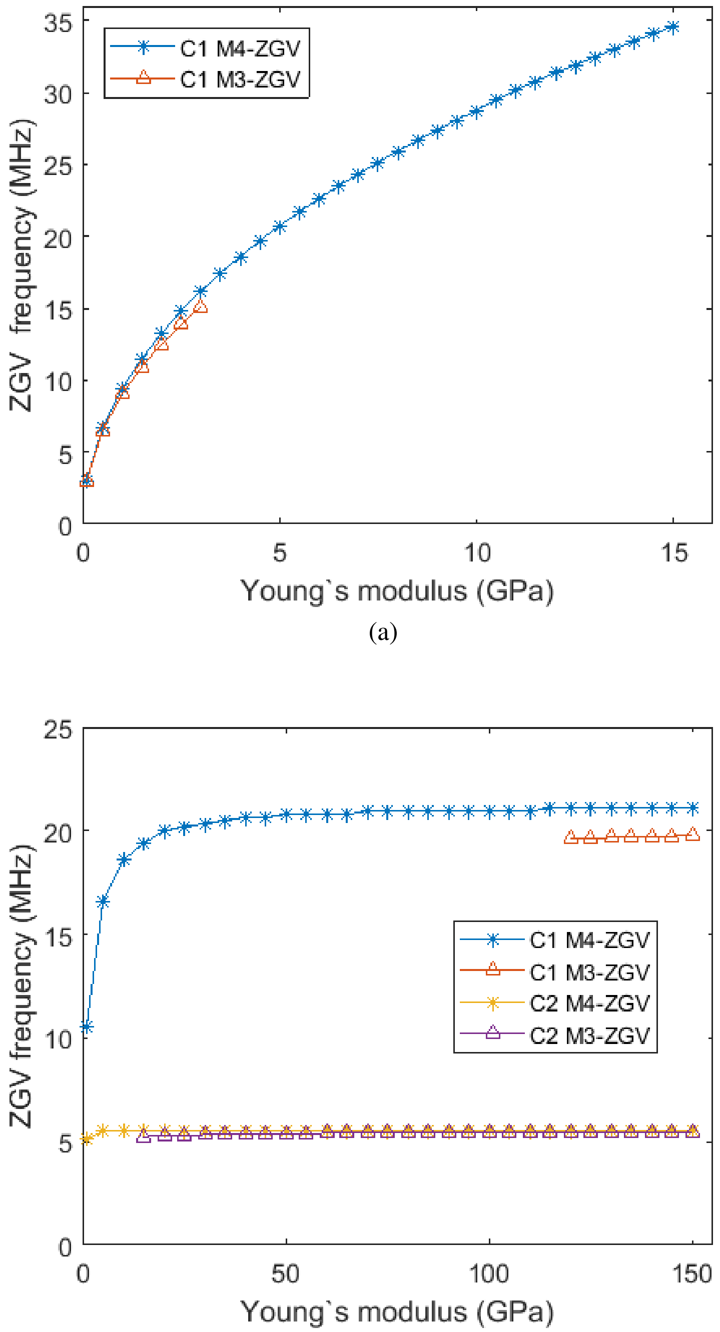

(a)

(b)

Figure 2.5: ZGV mode responses to changes of the Young's modulus of (a) the coating layer and (b) the current collector layer.

is stiffer. Figs. 2.4a and 2.4b show the M3-ZGV mode and M4-ZGV mode for comparison. For vertical displacement mode shapes, the M3-ZGV mode has similar displacement to the M4-ZGV

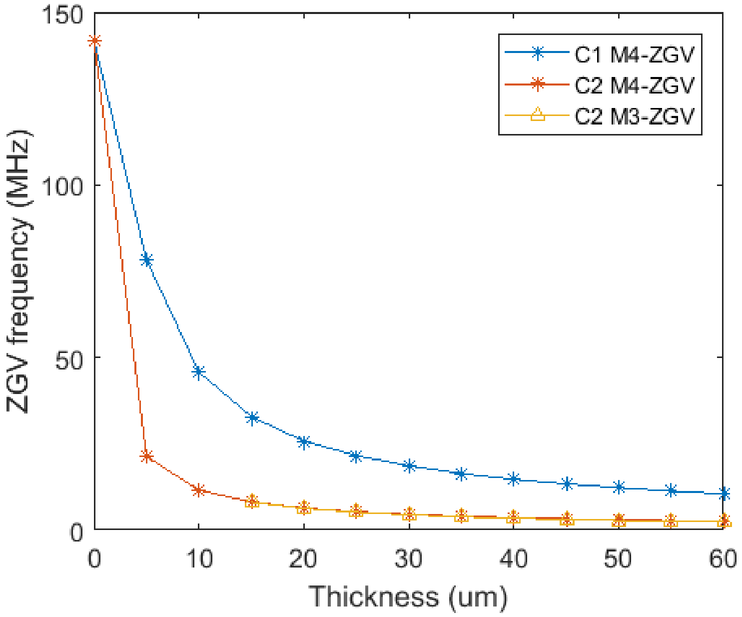

Figure 2.6: ZGV frequencies versus thickness of the coating layer in cases C1 and C2.

mode at the current collector surface and the battery coating surface. However, the M3-ZGV mode has noticeably higher displacement than the M4-ZGV mode at the current collector surface. For horizontal displacement mode shapes, the M3-ZGV mode has significantly higher displacement than the M4-ZGV mode at the battery coating surface, and very similar displacement at the current collector surface. Since the frequencies of the M3-ZGV mode and the M4-ZGV mode are very close to each other, and the M3-ZGV mode tends to have higher wavenumber k than M4-ZGV mode as shown in Fig. 2.2b, this indicates that the M3-ZGV mode has a shorter wavelength than the M4-ZGV mode. Shorter wavelength may be interpreted that less material may participate in the M3-ZGV mode than the M4-ZGV mode. However, distinguishing these modes would require very fine frequency resolution and a high signal-to-noise ratio in a measurement, additionally assuming that material damping would not broaden these modes so they appear coincident.

For a single layer structure, the frequency of the S1-ZGV mode can be estimated by

$$f_{S1-ZGV} = \frac{\beta V_l}{2h}, \tag{2.3}$$

where β is a correction factor which is often 0.96 [44]. $V_l/2h$ represents the cut-off mode ($k = 0$) of S1 mode created by longitudinal wave propagating only in the z direction. The cut-off mode is also called the thickness mode meaning the whole structure shown in Fig. 2.1 vibrates in the z direction harmonically. Similar methods can not be used for estimating M4-ZGV mode for a bilayer structure because the difference between the mechanical properties of each layer can cause different wave displacements and stress conditions in different layers as shown in Figs. 2.3 and 2.4. The M4-ZGV mode does not have the symmetry that the S1-ZGV mode has. For analyzing a bilayer structure consisting of two layers with very different mechanical properties, the simulation of dispersion curves is necessary to locate ZGV modes.

The following sections describe the sensitivity of the ZGV mode to variations in material parameters. It is significant that the M3-ZGV and the M4-ZGV modes have similar sensitivity in all cases.

The sensitivity of the ZGV modes to changes in Young's modulus (E_1 or E_2) was calculated. In Fig. 2.5, the M3-ZGV and the M4-ZGV modes responses for both cases C1 and C2 to changes of Young's modulus value of the battery coating layer (E_2) or the current collector layer (E_1) are shown. The geometry shown in Fig. 2.1 is used. In Fig. 2.5a, E_2 is simulated between 0.1 GPa to 15 GPa with an interval spacing of 0.5 GPa. In Fig 2.5b, E_1 is simulated between 1 GPa to 150 GPa with an interval spacing of 5 GPa. It is shown that the M3-ZGV and M4-ZGV modes increase monotonically for both cases when E_1 or E_2 increases. The M3-ZGV and M4-ZGV modes converge when E_2 is very low; they slightly diverge when E_2 increases. M3-ZGV disappears when E_2 is higher than 3 GPa and E_1 equals to 70 GPa for case C1 as shown in Fig. 2.5a. The M3-ZGV mode does not exist when E_1 is in the lower range close to E_2, but the M3-ZGV mode appears when E_1 is higher than 120 GPa for case C1 and 15 GPa for case C2. From Fig. 2.5, it is calculated that the M3-ZGV mode exists when the ratio of E_2/E_1 is greater than 4.2% for case C1 and 2.3% for case C2.

Fig. 2.5 also shows that the M3-ZGV and M4-ZGV modes are mostly determined by E_2 rather than E_1 when E_1 is sufficiently greater than E_2 . When E_2/E_1 is approximately less than 12% for case C1 and 6% for case C2, changes in E_1 will not result a significant shift in M3-ZGV and M4-ZGV modes as shown in Fig. 2.5b. Since increasing the Young's modulus of coating increases the acoustic bulk wave velocities (V_l and V_s) according to Eqs. 2.1 and 2.2, waves propagate through the structure in the z direction faster, resulting in ZGV mode frequency increases.

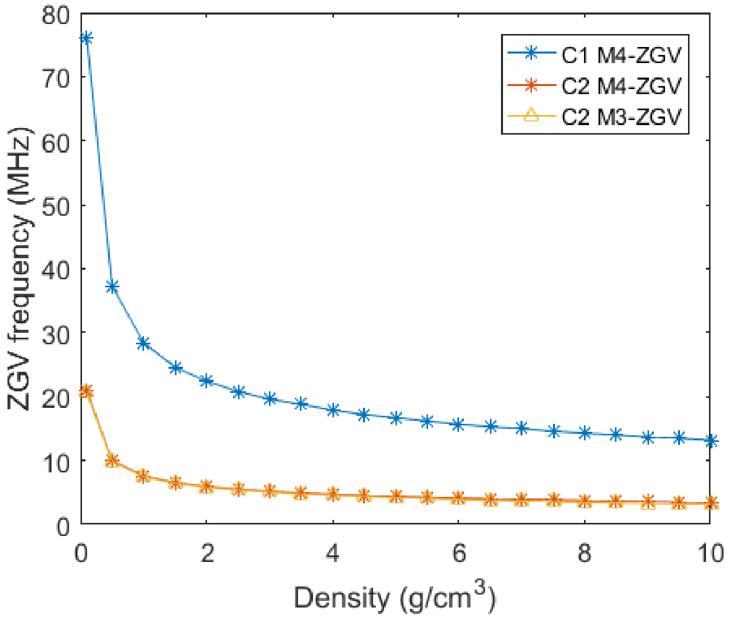

Figure 2.7: ZGV frequencies versus density of the coating layer in cases C1 and C2.

The sensitivity of the ZGV modes to changes in the coating thickness, h_2, and the results are shown in Fig. 2.6. The parameter h_2 is simulated between 0 µm to 50 µm with an interval spacing of 5 µm. M3-ZGV only appears for case C2. M3-ZGV and M4-ZGV modes decreases monotonically when the thickness of the coating layer increases. When acoustic bulk wave velocities are constant, increasing thickness increases the distance for acoustic bulk waves to travel through the whole structure in the z direction, resulting in lower frequencies of the ZGV modes.

The sensitivity of the ZGV modes to changes in the coating density, ρ_2, and results are shown in Fig. 2.7. The density range is simulated between 0.1 g/cm^3 to 10 g/cm^3 with an interval spacing of 0.5 g/cm^3. M3-ZGV only appears for case C2. Both the M3-ZGV mode and M4-ZGV mode decrease monotonically when the density of the coating (ρ_2) increases because the increasing coating density reduces the acoustic bulk wave velocities according to Eqs. 2.1 and 2.2. The decrease in the acoustic bulk wave velocities lengthens the time for waves to propagate through the structure in the z direction, resulting in decreasing frequencies of the ZGV modes.

In summary, ZGV modes are dependent on the geometry of the materials as well as the mechanical properties of the materials. In particular, the observed models show that ZGV modes

(M3-ZGV and M4-ZGV) are sensitive to the changes in mechanical properties of the coating material.

CHAPTER 3. EXPERIMENTS

There are different ways to measure Lamb waves using laser ultrasonic techniques. Most of the commercial laser vibrometer can only reach up to 10 MHz range. Other advanced commercial laser vibrometers are expensive and have many more features that are not necessary to this research. Therefore, we built up our own experimental setup. The setup we chose to use are commonly used by other researchers [17], [20], [21] to investigate ZGV Lamb waves.

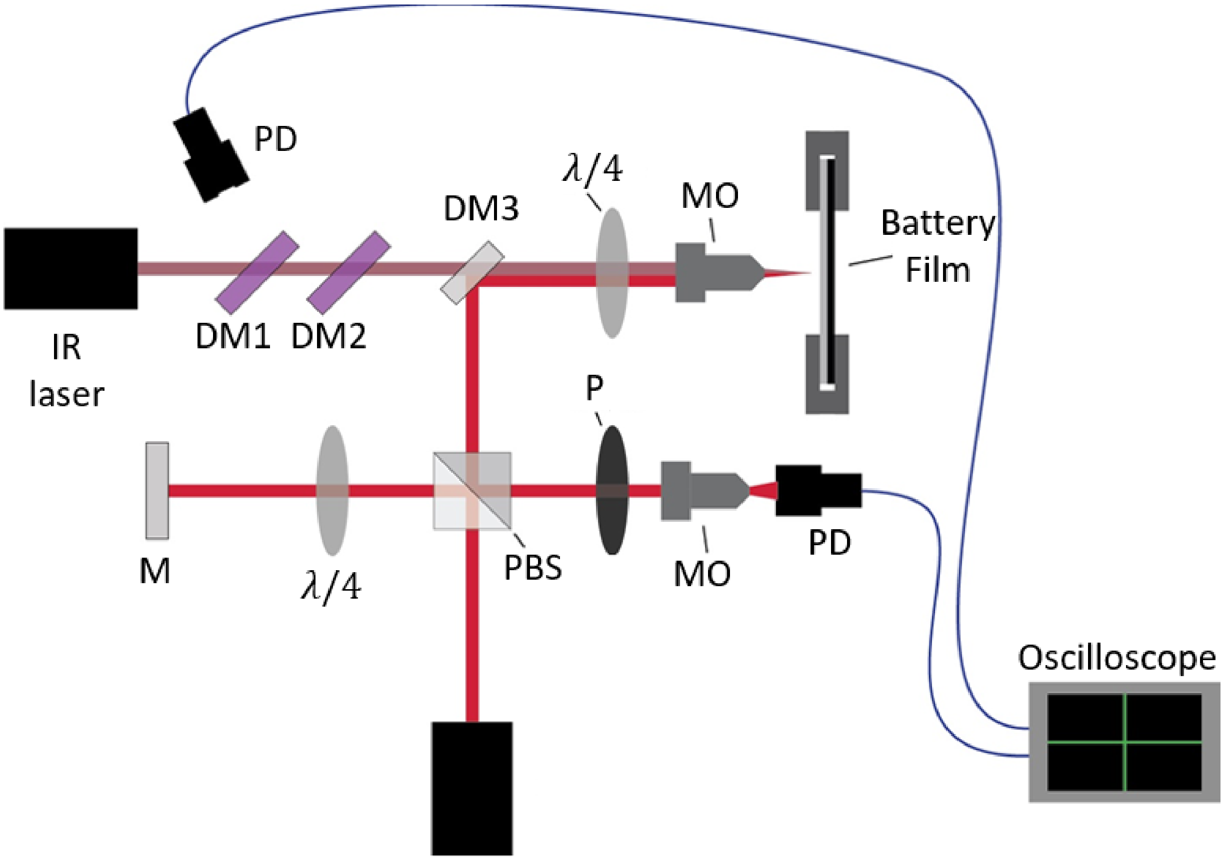

Figure 3.1: Schematic of the experimental setup. The components of a homo-dyne interferometer are labeled as DM1,2,3: dichroic Mirrors, PBS: polarized beam splitter, $\lambda/4$: wave retarder plate, M: mirror, MO: microscope objective, P: polarizer, PD: photo-diode

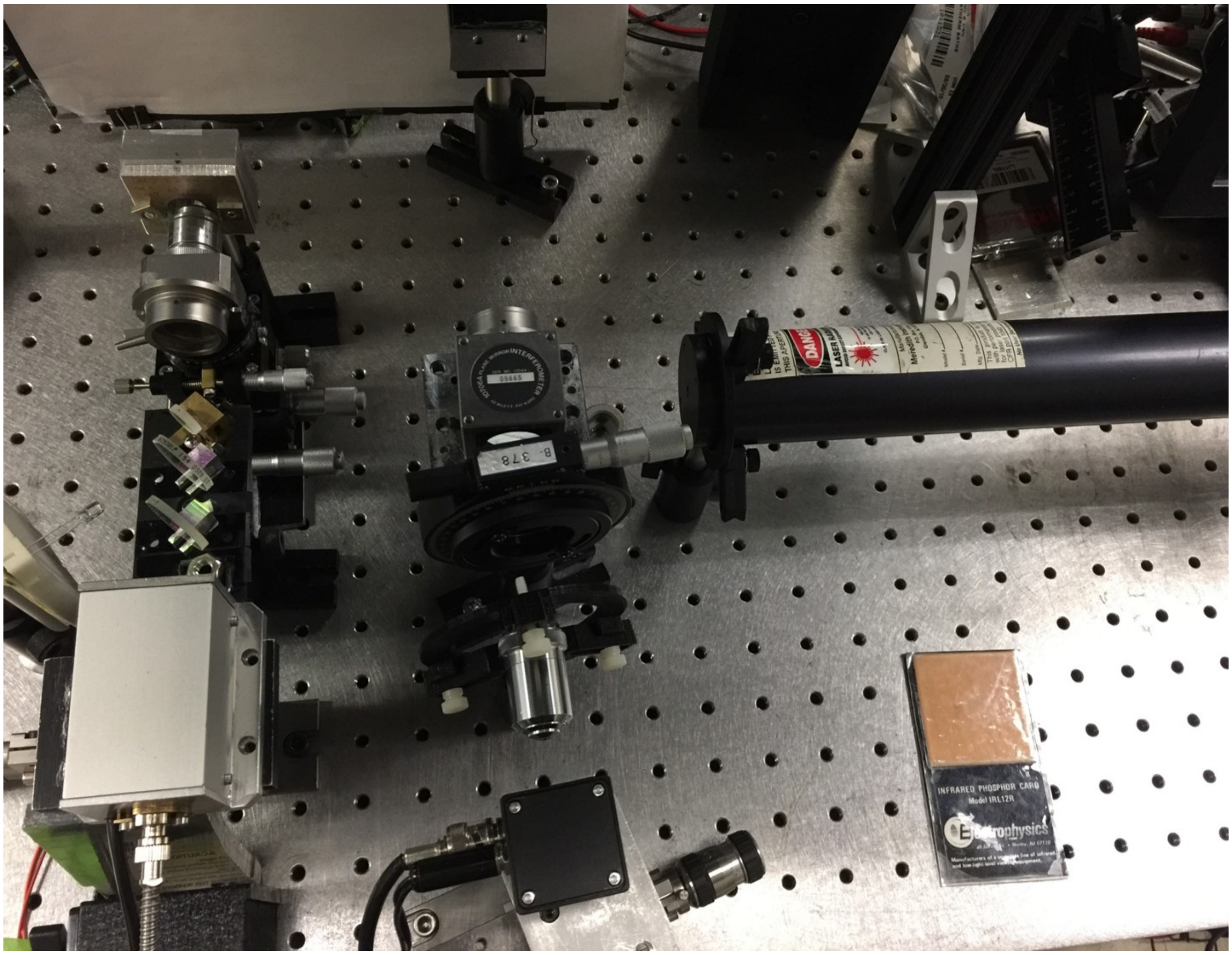

Figure 3.2: Photo of the full experimental setup shown in Fig. 3.1

3.1 Experimental Setup

A diagram of the experimental arrangement is shown in Fig. 3.1. A photo of the experimental setup is shown in Fig. 3.2. The pump laser source is an ultra-fast diode-pumped-solid-state (DPSS) Infrared (IR) laser (Standa STA-001) with an optical wavelength centered at 1050 nm. This pulsed laser provides a pulse energy around 600 µJ within a 500 ps duration with a pulse repetition rate up to 50 Hz. Due to the high power of the pump laser pulse, two identical dichroic mirrors (DM1,2: Omega Optics EB00479B) with a 20% transmitting rate for IR light at 1050 nm are used as a diffuser to sufficiently attenuate the energy focused on the current collector in order to avoid laser ablation of the metal films or the battery coatings. The detection laser is a polarized Helium-Neon laser (Uniphase 3067) with a rated power of 10 mW and an optical wavelength centered at 632.8 nm.

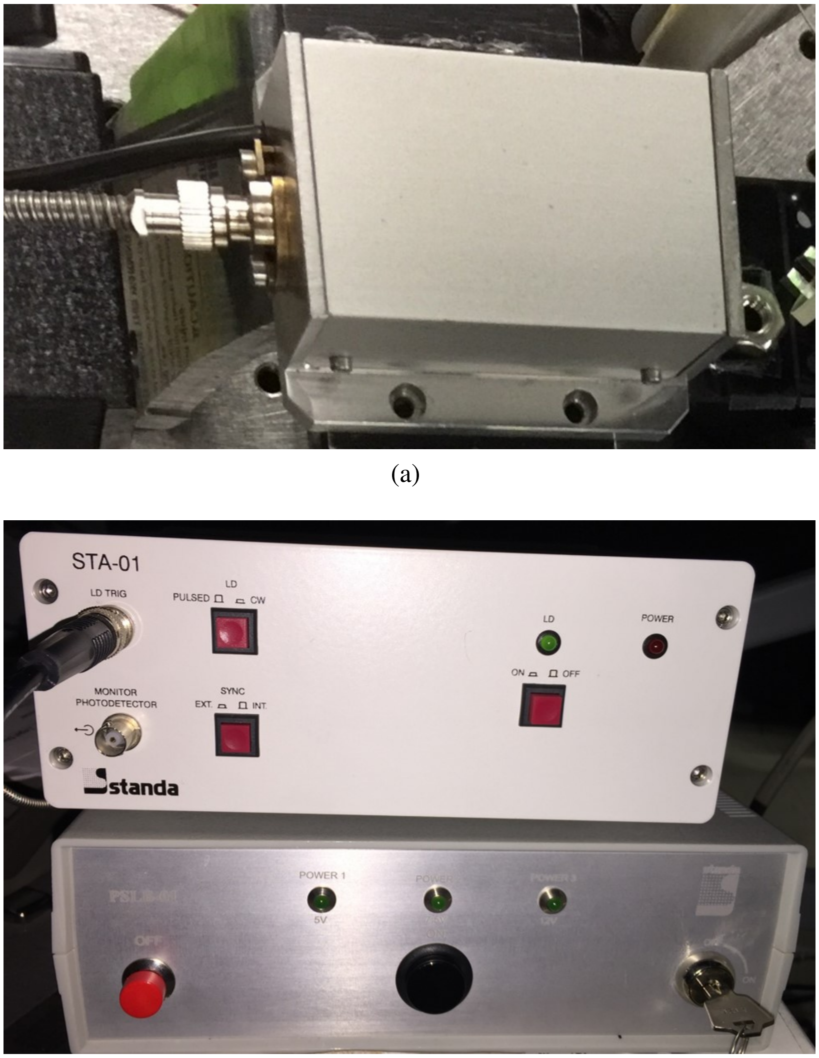

(a)

(b)

Figure 3.3: Photo of the IR laser used in Fig. 3.1. (a) The laser head. (b) The power supply.

In this homodyne interferometer, two quarter wave plates (Newport 10RP0424) and a polarized beam splitter (Newport, 10BC16PC4) are used as a circulator to avoid retro-reflection of the Helium-Neon laser which can cause unpredictable power changes. The detection laser gets reflected while the pump laser goes through a dichroic mirror (DM3: Thorlabs DMLP900T) which has a 98% reflection coefficient at wavelength 632.8 nm and 96% transmission coefficient at wavelength 1050 nm. Both the detection laser and pump laser are focused on the testing sample by a microscope objective (Newport M-10×) with 10× magnification. The beam spot sizes of the detection laser and pump laser are approximately 3 μm and 5 μm respectively. The interferometer signal beam and reference beam are combined and pass through a polarizer (Newport 5511) at 45° to show the interference pattern. Another microscope objective (Newport M-60×) with 60× magnification is used to expand the beam in order to observe the interference pattern during alignment procedures.

(a)

(b)

Figure 3.4: Photo of the Helium-Neon laser used in Fig. 3.1. (a) The laser head. (b) The power supply.

3.2 Processing

The interferometric signal from the sample is recorded by a fast amplified photo-detector (Newport 818BB21A) with a bandwidth from 30 kHz to 1.2 GHz and sampled by an oscilloscope (Lecroy WaveRunner 204Xi) using DC 50 Ω coupling. The oscilloscope is triggered with a photo-diode (Vishay 7511001ND) detecting the pump laser pulse and then records 2 μs of signals, consisting of 0.2 μs in pre-triggering and 1.8 μs in post-triggering. The oscilloscope sampling rate is set at 5 Gs/s. A preprocessing digital low-pass filter with a bandwidth of 151 MHz is applied to lower the noise level. The recorded signals are coherently averaged 2000 times in the time domain to increase the signal to-noise-ratio (SNR). Since the pulsed laser repetition rate is 50 Hz, this whole process takes about 1 minute to measure one physical location on the sample film. The averaged data is transformed into the frequency domain in MATLAB, using a Fast Fourier Transform (FFT) with a Hann window, to compute the power spectral density. Resonances are recognized by finding peaks in the power spectral density. The value of the peak frequency is determined as the mean of the Gaussian curve fitted to the peaks in the power spectral density.

The oscilloscope and the fast amplified photo-detector are shown in Figs. 3.5 and 3.6.

Figure 3.5: Lecory WaveRunner 204 Xi

3.3 Testing Procedures and Testing Samples

All measurements were performed at room temperature. Samples were clamped by two aluminum plates ($6 \times 6 \times 3$ cm^3) with a 1.5 cm diameter circular cutout in the center of. The tested electrodes were cut into small pieces (2×2 cm^2) from the original electrode films to fit between the two aluminum plates. The two aluminum plates were clamped together using screws and were

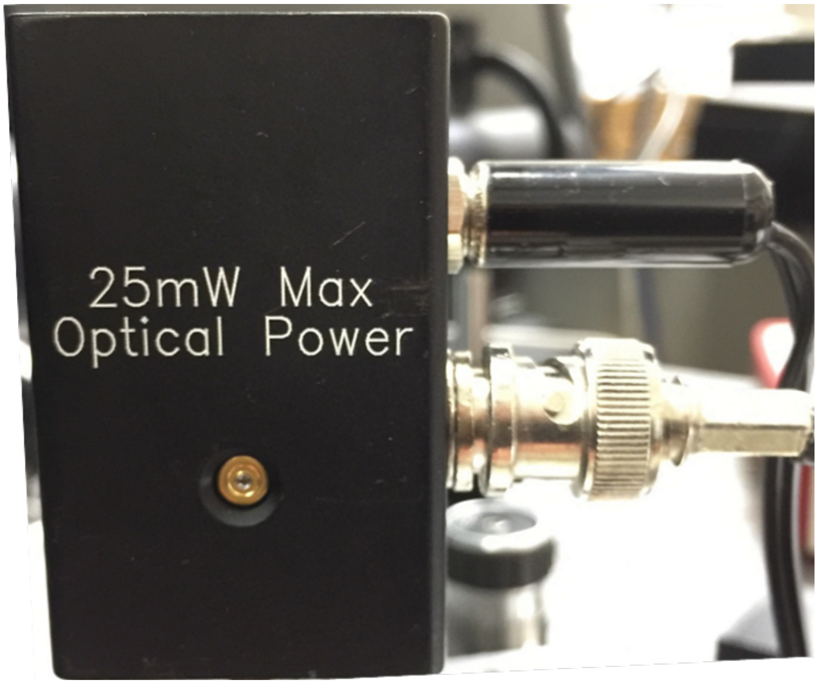

Figure 3.6: Newport 818BB21A

slightly tightened together, just enough to hold the film rigidly. Photos of the clamp used in this work is shown in Fig. 3.7. The pump laser was first approximately aligned by using a IR sensor card (Newport F-IRC1) to check if the IR laser beam and detection laser beam were overlapping behind the microscope objective (M-10×). Then the IR laser was aligned more carefully by minimizing time-of-flight of the first acoustic arrival (the highest displacement) after the IR pulse. By doing so, the excitation and detection points were approximately at the same point where the ZGV Lamb modes would exist. These procedures were repeated for each measurement at different spots on each sample. Visual inspection was used to confirm the ZGV modes were generated without any ablation of the electrode films.

The tested samples of different battery electrode films and current collectors are shown in Table 4.2. The corresponding mechanical properties of the coating of battery films are shown in Table 4.1. The notation (uncal) indicates the samples were not calendered. The film thickness was that reported by the manufacturer. The density of the battery coating was estimated by dividing the measured mass by the estimated volume. The Poisson ratio was assumed to be the common value 0.3 [39]. Each sample was tested at 5 different random spots to obtain the mean and standard deviation of the ZGV frequency response of each film.

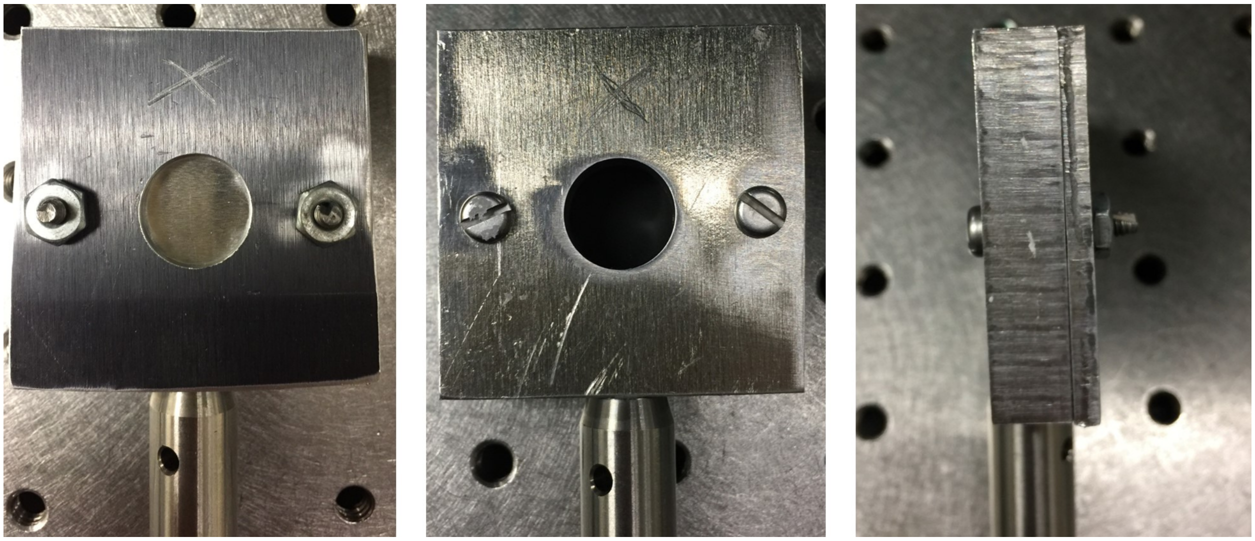

Figure 3.7: Photos of the clamp used in this work.

The calendering apparatus is shown in Fig. 3.9. By adjusting the gap between the two cylinders, the battery films were calendered to desired thicknesses. To avoid delamination of the battery coating layer, during the calendering process the films were calendered several times by steady reduction of the gap between the cylinders until the desired thickness was achieved. Thickness were measured with a micrometer (Mitutoyo IP65) with 0.001 mm resolution. Cathode 1 (uncal) was cut into square samples. To obtain a sequence of measurements during a calendering process, one sample went through a series of 10 cycles of (1) calendering, (2) thickness measurements, and (3) ZGV measurements. Other samples were calendered into a different thickness in one step, after which the thickness was measured followed by ZGV measurement. A photo of the calendering apparatus is shown in Fig. 3.10. The micrometer used in this work is shown in Fig. 3.8.

To validate that the estimated Young's modulus of the battery film coating using the ZGV frequency was on the correct order-of-magnitude, we performed compression test using a universal testing system (Instron 3345) to measure the Young's moduli of Cathode 1 and Cathode 1 (uncal). These two films were cut into many pieces each approximately 8 mm×8 mm and then stacked up together as shown in Fig. 3.12. 18 pieces of Cathode 1 and and 20 pieces of Cathode 1 (uncal) were used in these tests. The universal testing system (Instron 3345) is shown in Fig.3.11. Fig. 3.13 shows the the films under compression.

Figure 3.8: A photo of micrometer.

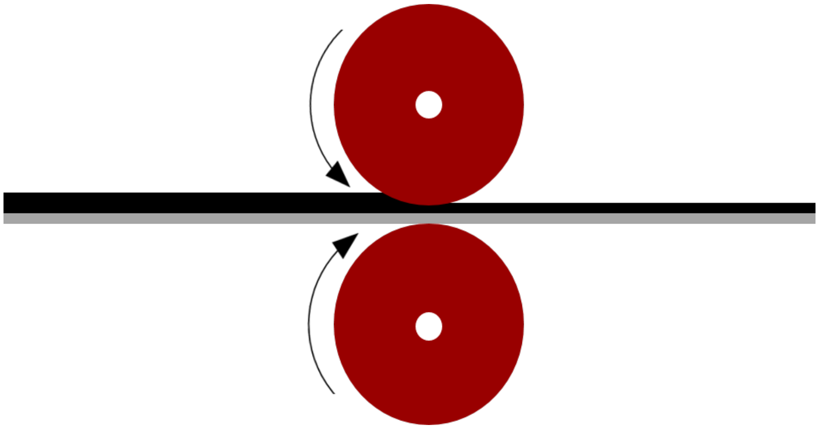

Figure 3.9: A schematic of the calender setup.

Figure 3.10: A photo of calendering apparatus.

Figure 3.11: The universal testing system used in this work.

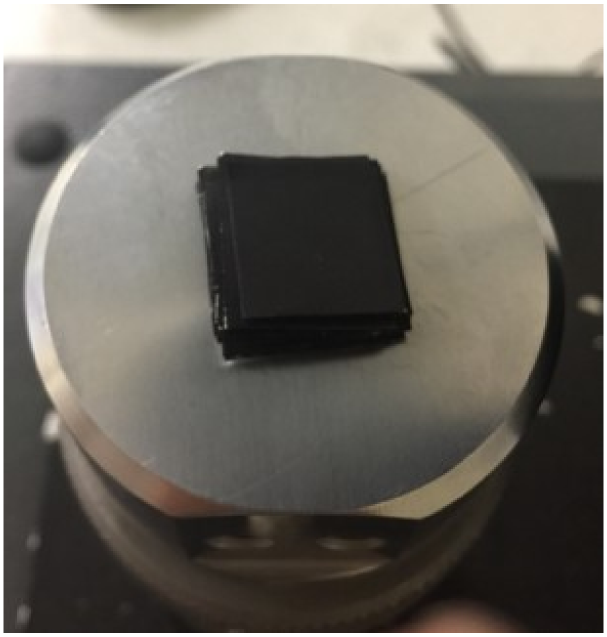

Figure 3.12: Samples on the holder before compressing.

Figure 3.13: Samples between the holders while compressing.

CHAPTER 4. RESULTS

4.1 Battery Films

The averaged ZGV measurements (from 2000 pulses) and the associated power spectral densities of a reading of noise, Cathode 1 and Anode 1 are shown in Figs 4.1, 4.2 and 4.3, respectively. There is a high voltage short duration jump denoted as an IR pulse in the time domain. This IR pulse generates a systematic peak in the power spectral density at approximately 21 MHz. The ZGV frequencies are at 22.5 MHz for Cathode 1 in Fig. 4.2 and 6.5 MHz for Anode 1 in Fig. 4.3. Except for the systematic IR peak in the power spectral density, only a single peak was observed in each battery film measurement.

The ZGV frequencies of different commercial-grade battery films and an aluminum current collector are shown in Table 4.2. A copper current collector was not measured because the ZGV frequency was higher than the bandwidth of our experimental setup. The resonance frequencies are shown as f and s.d.f representing the estimated mean and the standard deviation, respectively. The estimated wavelength of each ZGV mode is calculated by fitting the measured ZGV frequencies to simulated dispersion curves. The Young's modulus values of the battery coatings are calculated by fitting the experimental results in Table 4.2 to the theoretical models (discussed below).

Table 4.1: Measured and calculated mechanical properties of commercial battery electrode coating in this work.

Coating	$\rho(\mathrm{g/cm^3})$	h(µm)	ν	E(GPa)	s.d.E(GPa)
Anode 1	1.407	45	0.3	0.90	0.10
Cathode 1(uncal)	1.390	46	0.3	1.12	0.04
Cathode 1	2.460	26	0.3	6.09	0.14
Cathode 2(uncal)	2.137	53	0.3	3.20	0.20

Table 4.2: Measured ZGV frequencies and corresponding wavelengths of different battery films and current collector.

Material	f(MHz)	s.d.f(MHz)	λ(μm)	s.d.λ(μm)
Anode 1	6.00	0.32	229.93	6.95
Cathode 1(uncal)	7.05	0.19	253.80	8.72
Cathode 1	22.80	0.25	317.17	4.89
Cathode 2(uncal)	9.75	0.29	673.85	3.41
Aluminum	146.20	1.11	10.61	0.04
Al(Cathode 1)	147.20	0.44	10.63	0.03
Al(Cathode 2(uncal))	145.00	0.27	10.53	0.02

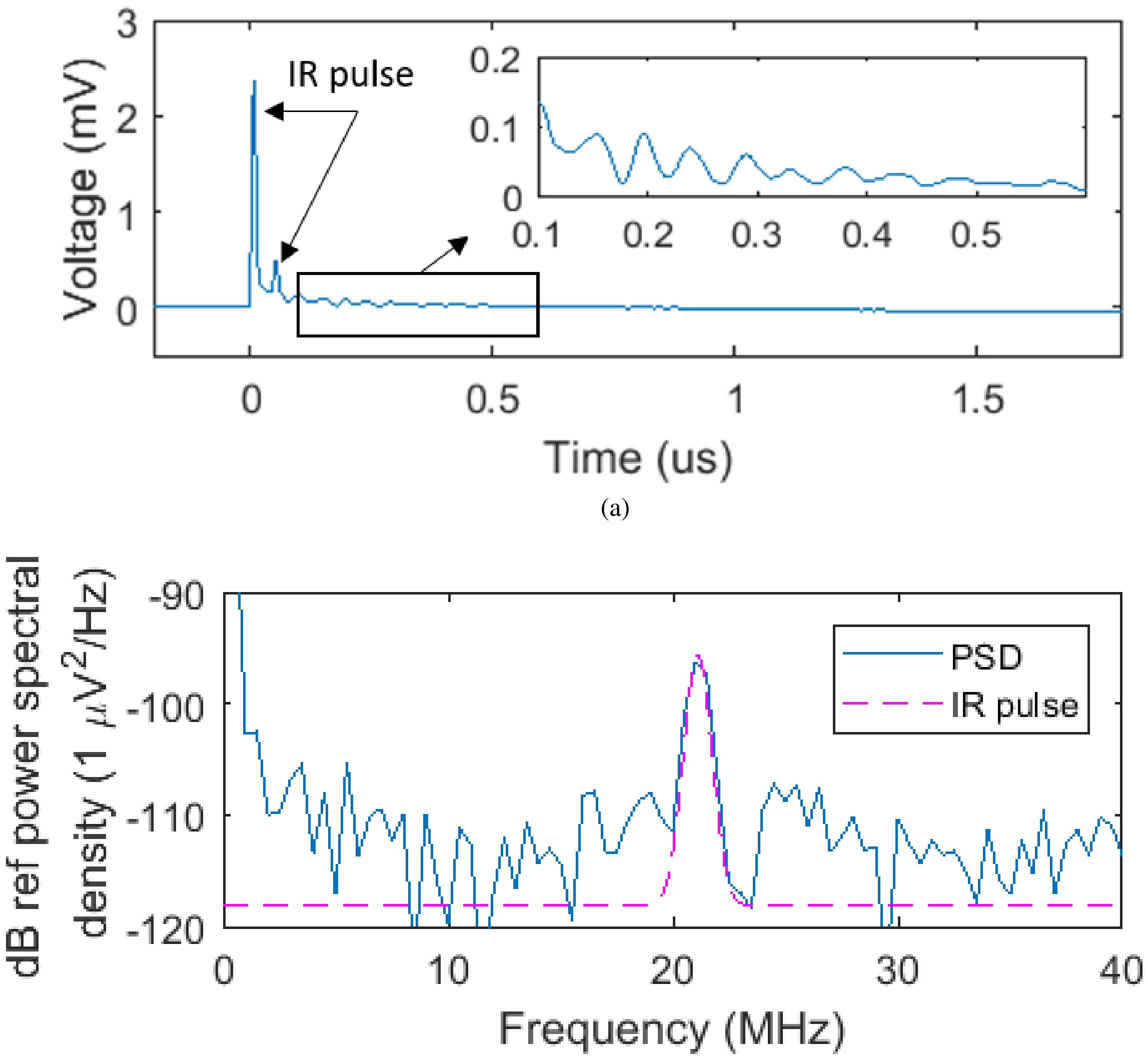

(a)

(b)

Figure 4.1: Experimental measurement of noise baseline in the (a) time domain and its (b) computed power spectral density taken when the detection laser is off. The dashed line shows the Gaussian fit used to estimate frequency information.

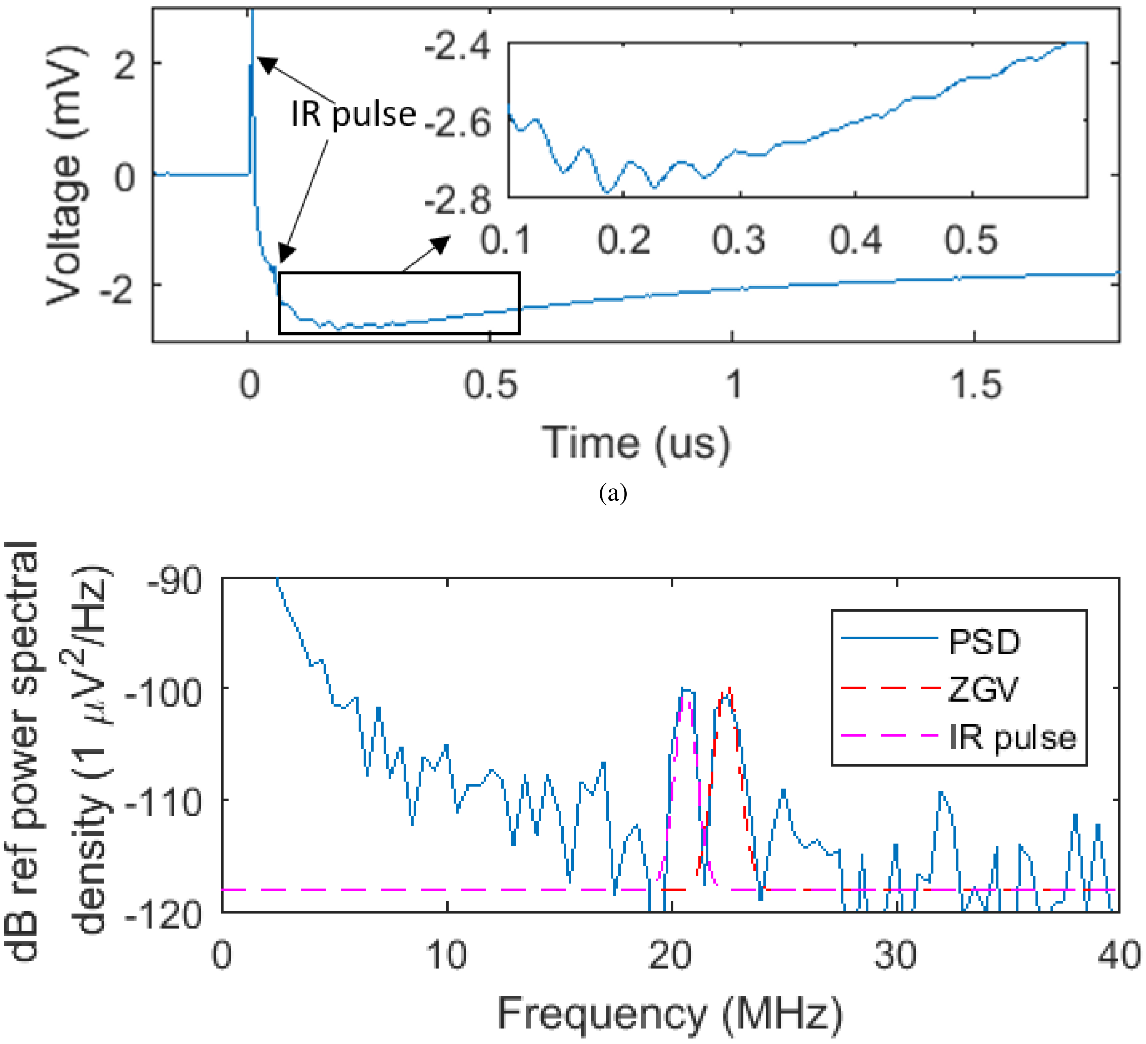

(a)

(b)

Figure 4.2: Experimental measurement of Cathode 1 in the (a) time domain and the (b) computed power spectral density.

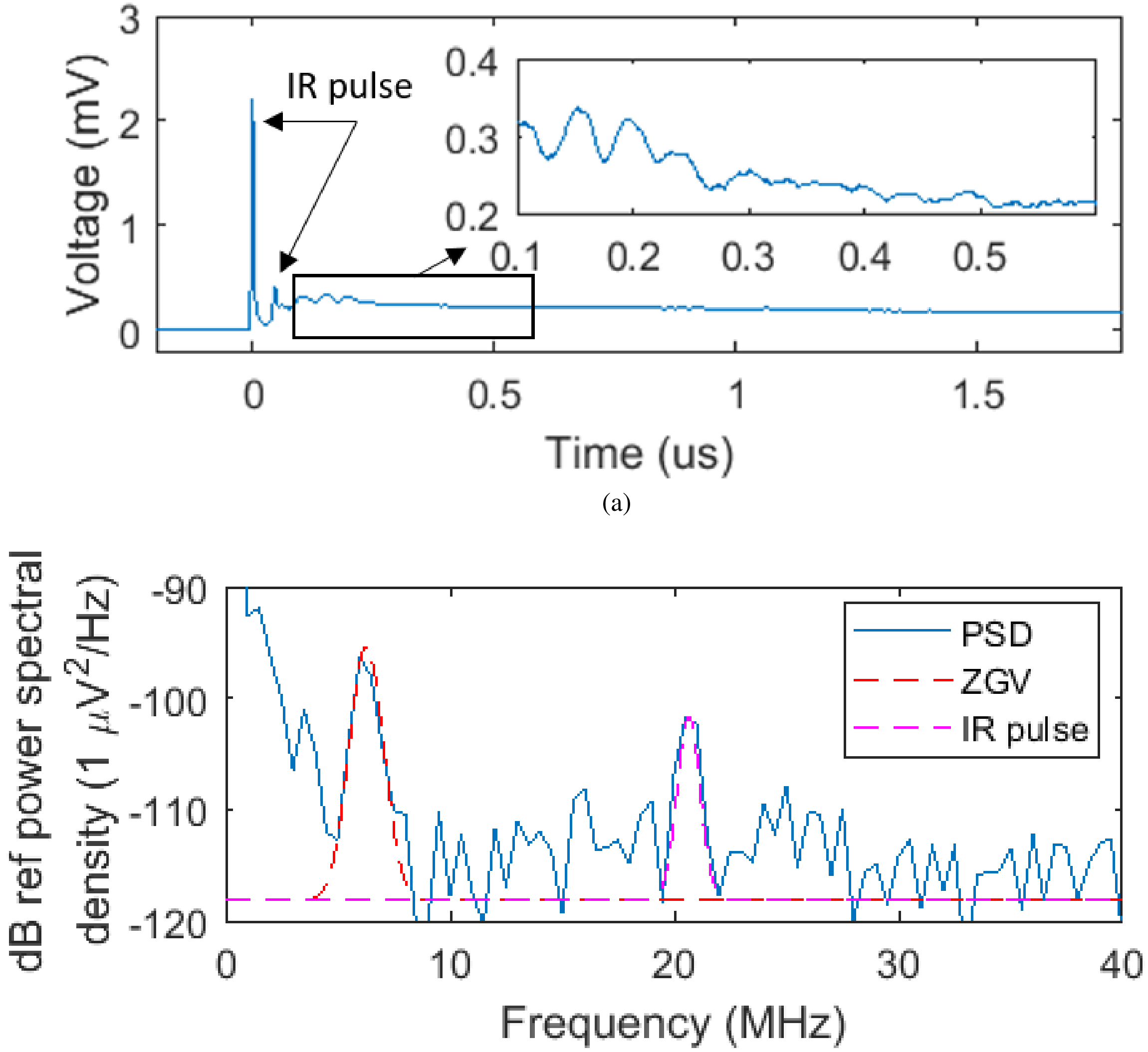

(a)

(b)

Figure 4.3: The experimental measurement of Anode 1 in (a) time domain and (b) power spectral density.

4.2 Calendering Test

The calendering test results are shown in Fig. 4.4. Changes of the resonance frequencies are seen during the calendering process. Error bars are estimated using a 95% confidence interval. It is clear that the ZGV frequencies change significantly during the calendering process. The resonance frequency first drops by 2.23 MHz and then increases as the samples are calendered into thinner thickness. It is noted that the ZGV frequency of Cathode 1, which was calendered by the manufacturer, is significantly higher than ZGV frequency of Cathode 1 (uncal) that was calendered in our laboratory to the same apparent thickness (Sample 5 in Fig. 4.4).

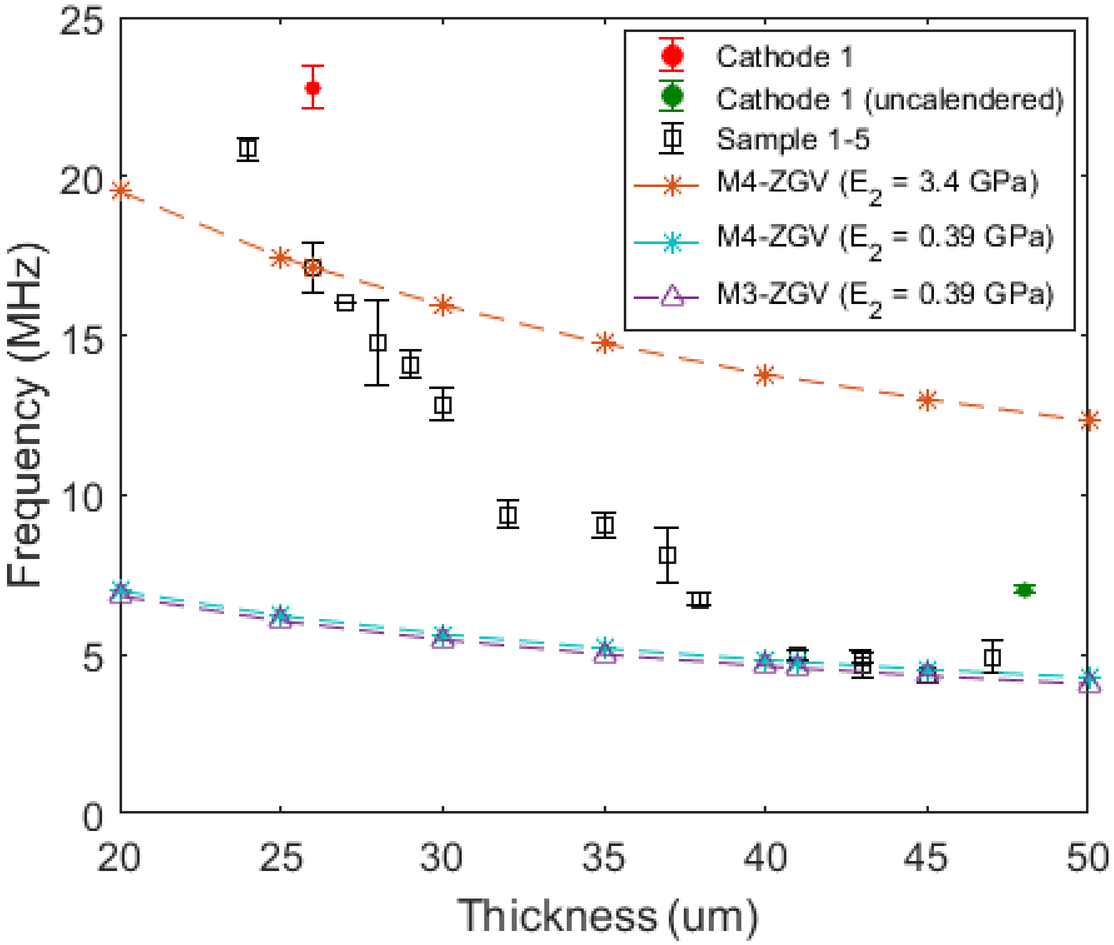

Figure 4.4: The ZGV resonance frequency results from cathode 1 (uncal) calendering test.

CHAPTER 5. DISCUSSION

5.1 Thickness Estimation of Current Collectors

As shown in Table 4.2, the S1-ZGV mode of the current collectors of different cathodes has a 95% confidence interval at 146.20 ± 0.79 MHz. The simulated result for a 20-µm-aluminum sheet is 142 MHz using the mechanical parameters in Table 2.1. The thicknesses of the current collectors can be extracted from measured S1-ZGV frequencies [20].

The S1-ZGV modes of the current collectors of Cathode 1 and Cathode 2 (uncal) are different from the predicted value in Table 4.2. The estimated thickness of current collector of Cathode 1 is 19.55 ± 0.02 µm, and the estimated thickness of current collector of Cathode 2 (uncal) is 19.31 ± 0.09 µm. The thickness measured from micrometer is the same as the reported value from the manufacturer at 20 µm. The estimated thicknesses for the current collectors from the ZGV measurement agree very well (within 2.9%) with the measurement from the micrometer and the manufacturer. The experimental results show that the ZGV measurement is accurate for measuring the thickness of current collectors.

5.2 Young's Modulus Estimation of Battery Coating

The Young's modulus of the battery coating layer can be estimated from the measured ZGV frequencies. According to Chapter 2, the frequencies of the M3-ZGV mode and the M4-ZGV mode are very close to each other (less than 1 MHz difference). Our ZGV measurement has a resolution at 0.5 MHz. Damping additionally widens the spectral peaks. The difference between M3-ZGV mode and M4-ZGV mode thus are within the uncertainty of the systematic error from our experimental setup. Since the M4-ZGV mode exists in all the simulations in Chapter 2, and is not dependent on the Young's modulus difference between the two layers, we chose the M4-ZGV mode as the measured ZGV resonance.

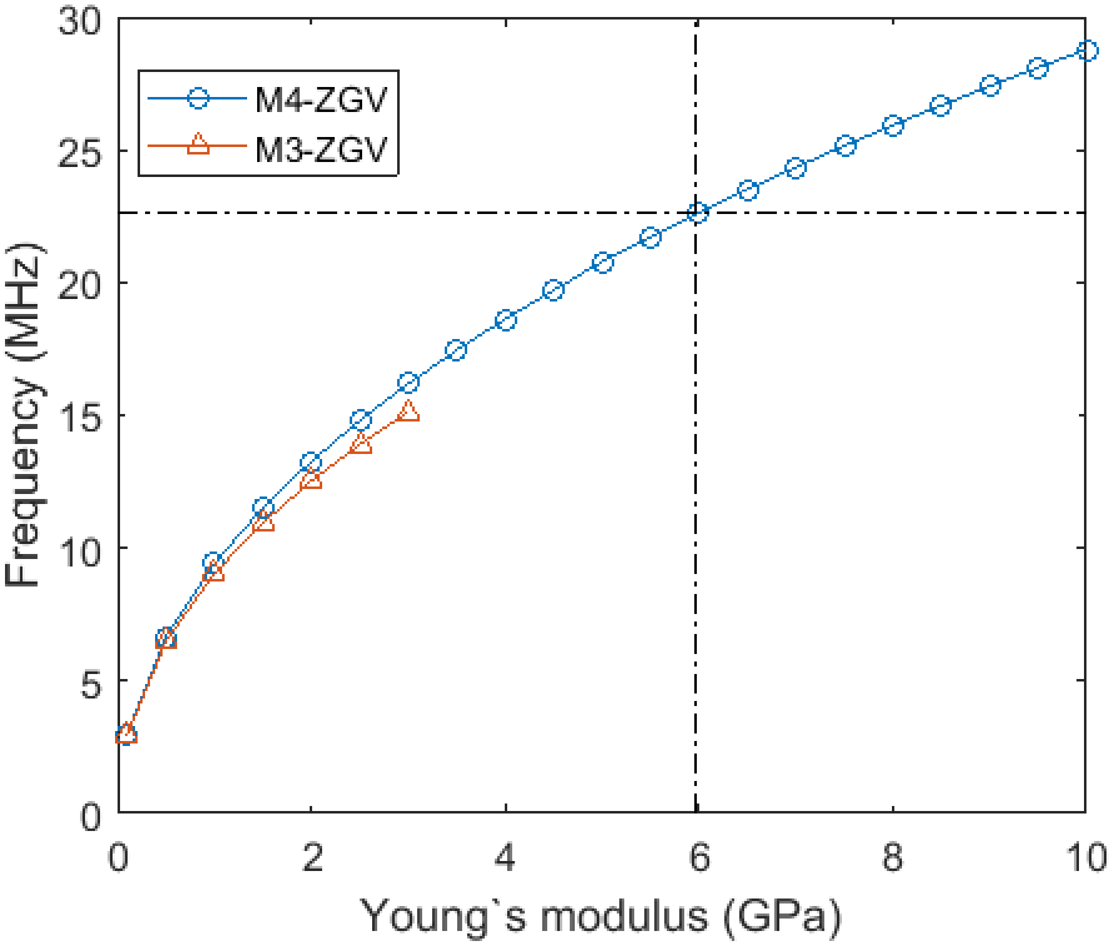

Figure 5.1: The Young's modulus estimation of the coating of Cathode 1. The mechanical properties listed in Table 4.1 are used in simulation. The estimated Young's modulus is 5.97 GPa when the ZGV frequency is at 22.6 MHz.

A wide range of the Young's modulus value were used to generate the numerical relationships between the Young's modulus and the ZGV mode frequency. The measured ZGV frequencies are fitted to the simulated ZGV mode in order to estimate the Young's modulus of the coating. An example of estimation process is shown in Fig. 5.1. The estimated Young's modulus is estimated to be 5.97 GPa when the ZGV frequency is 22.6 MHz

The estimated Young's modulus results for the coating of the measured battery film samples are listed in Table 4.1. For each sample, the measured ZGV frequencies of the 5 interrogated positions were used individually to estimate the corresponding Young's modulus at each spot. The mean and standard deviation (s.d.*E*) of the estimated Young's modulus was then calculated for each film sample. The results indicate that the frequency of ZGV Lamb modes is very sensitive and accurate (resolution at hundreds of MPa) to changes in the Young's modulus of battery film coatings.

After the Young's modulus is estimated, the corresponding wavenumber k can be determined by examining the dispersion curve associated with that ZGV mode. From these wavenumbers the corresponding wavelengths for each battery film sample are shown. The results of the calculated wavelengths for each battery film are shown in Table 4.2. Anode 1 has the shortest wavelength around 200 µm. Cathode 2 (uncal) has the longest wavelength around 700 µm. The wavelength results demonstrate that the ZGV measurement is localized to an approximately 1×1 mm^2 area of the film. This area of interrogation is on the same order as other measurements of heterogeneity [45]. The measured area can be assumed to be an infinite plane until its position near the edge of the clamp boundary is on the same order as the ZGV mode wavelength. [46] This indicates that the measurement can be performed without the concern of the boundary conditions of the clamp shown in Fig. 3.1.

To validate that the estimated Young's modulus of the battery film coating using the ZGV frequency was on the correct order-of-magnitude, we performed compression test using a universal testing system (Instron 3345) to measure the Young's moduli of Cathode 1 and Cathode 1 (uncal). These two films were cut into many pieces each approximately 8 mm×8 mm and then stacked up together as shown in Fig. 3.12. 18 pieces of Cathode 1 and and 20 pieces of Cathode 1 (uncal) were used in these tests. The force (N) to displacement (ΔL) relationships of Cathode 1 and Cathode 1 (uncal) are shown in Fig. 5.2. The Young's modulus is calculated using $E = (FL)/(A\Delta L)$, where F is the force, L is the thickness of the battery coating, A is the area. Since the Young's modulus difference between the battery coating and aluminum is very high, we assume that only the battery coating is compressed during the test. The estimated Young's modulus from the compression experiment us 1.65 ± 0.41 GPa for Cathode 1 and 0.38 ± 0.23 GPa for Cathode 1 (uncal). The estimated Young's moduli from these compression experiments have the same order-of-magnitude with estimated Young's moduli from the ZGV measurement.

The Young's modulus values of different battery films apparently have been measured from the MPa into the GPa range [10], [47], [48]. Forouzan *et al*. [47] measured the elasticity of coating (delaminated from the current collector) to be about 11.3 MPa. Nadimpalli *et al* [48]. calculated the elasticity of a cathode coating to be about 40 GPa using the rule of mixtures. Dallon *et al* [10]. estimated the elasticity of the coating of three different cathodes from 0.344 GPa to 5.04 GPa using acoustic measurements. The Young's modulus values estimated from the ZGV measurement are comparable to the measured results of Dallon *et al*. The measured elasticity difference of Cathode 1 is within 20% of the previously estimated value by the alternative method.

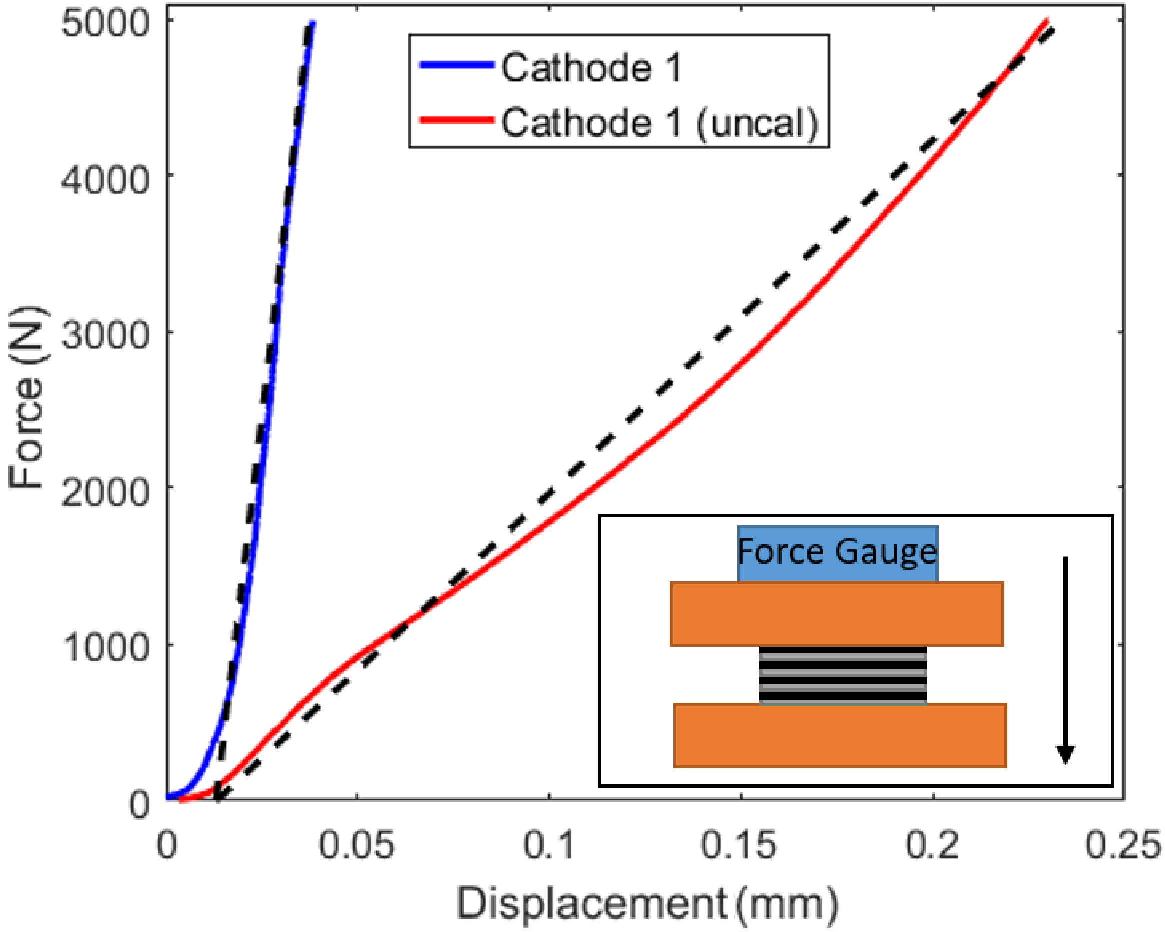

Figure 5.2: Force to displacement relationships of cathode 1 (blue dotted line) and cathode 1 (uncal) (red dotted line). The dashed lines are the used to fit the relationships to find ΔL. A diagram of the universal testing system is shown in the sub-figure.

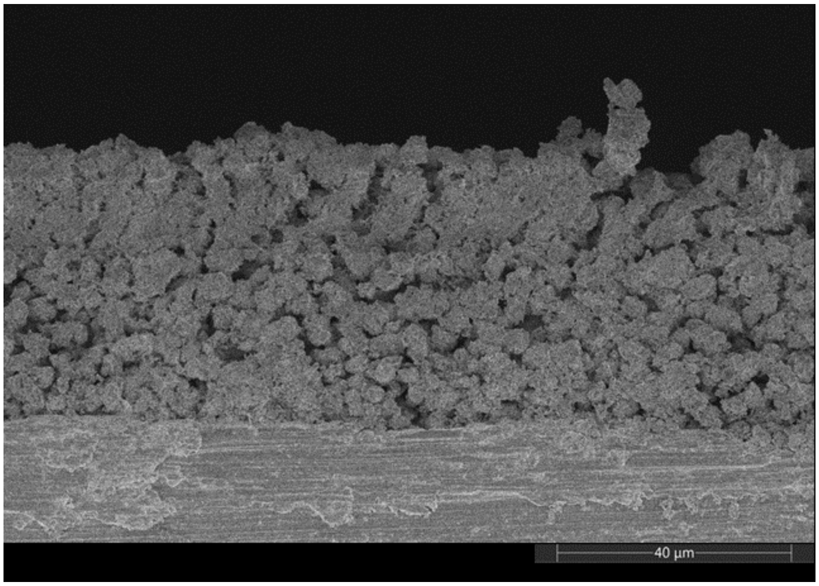

Figure 5.3: Scanning electron microscope micrograph of the cross section of Cathode 1 (uncal) with coating thickness of 48 µm.

5.3 Mechanical Properties Change During Calendering Process

Calendering is an important manufacturing step before battery films are packaged into cells. After the battery coating is dry, the coating layer surface is rough. Surface bumps and valleys have elevation differences of a few micrometers. In Fig. 5.3, the estimated thickness variation of the coating surface is approximately 4 µm. The porosity and density of uncalendered coatings are not optimal for battery performance [49], [50]. The calendering process can flatten the rough surface, increase the coating density, and decrease the porosity of the coating layer as shown in Fig. 5.4 and Fig. 5.5.

When the coating layer is calendered, the coating density increases, The density is estimated using

$$\rho = M_A/h, \tag{5.1}$$

where M_A is a constant representing the loading of the coating, mass per unit area.

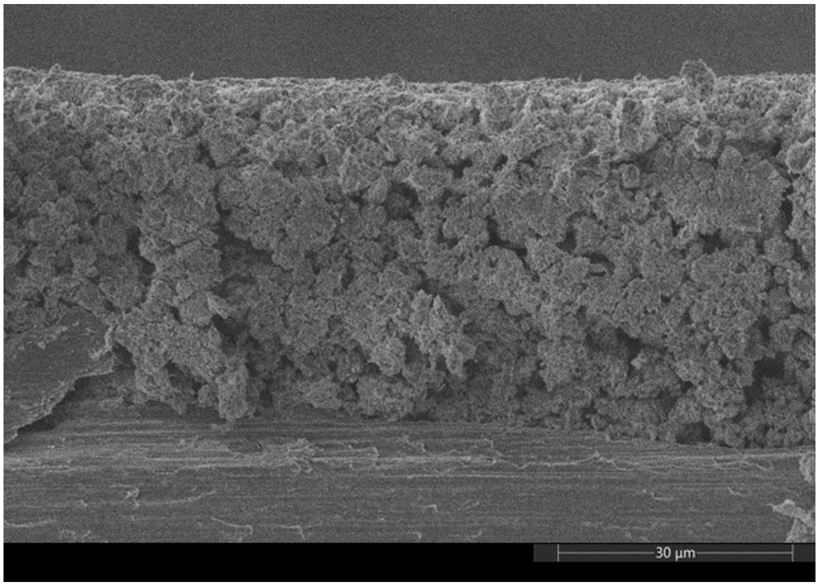

Figure 5.4: Scanning electron microscope micrograph of the cross section of Cathode 1 (uncal) with coating thickness calendered to 45 µm.

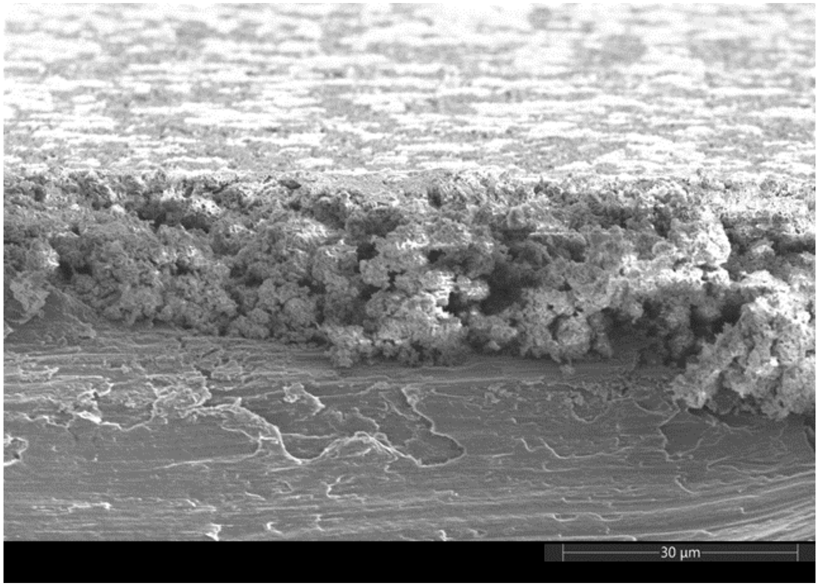

Figure 5.5: Scanning electron microscope micrograph of the cross section of Cathode 1 (uncal) with coating thickness calendered to 26 µm.

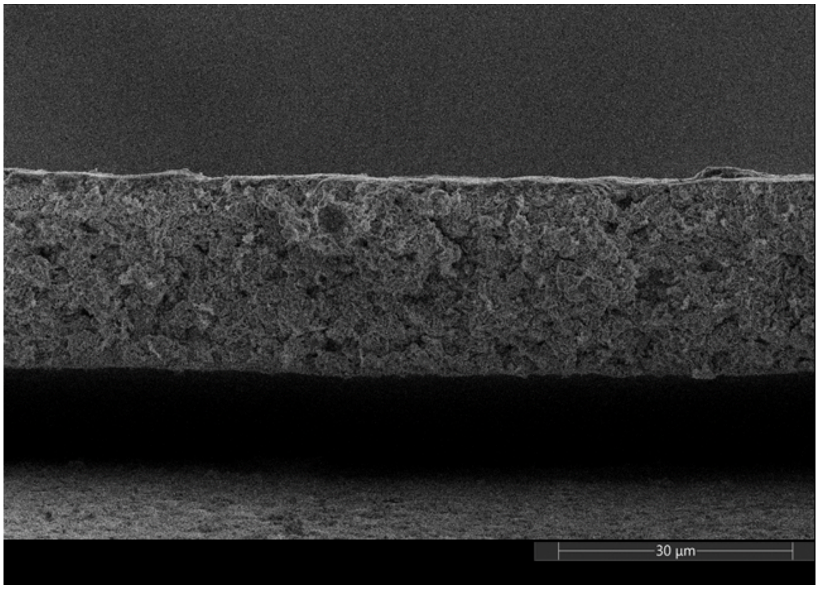

Figure 5.6: Scanning electron microscope micrograph of the cross section of Cathode 1 (calendered by the manufacturer) with coating thickness of 26 µm.

Figure 5.7: A diagram to show the effective thickness change during the first few calendering processes. The brown layer, black layer and gray layer represent the mass loading layer, effective coating layer and current collector layer, respectively

Fig. 4.4 shows that when Cathode 1 (uncal) coating was first calendered into a slightly thinner thickness (from 48 µm to 45 µm), the ZGV frequency decreased. A plausible explanation for this phenomenon originates in the rough surface and pores randomly distributed across the coating layer. Some large pores estimated from Fig. 5.3 are more than 19 µm in length and 1 µm in height. Lamb waves will not propagate efficiently through the pores because of the impedance mismatch between the pore air and coating material. This leads to a modal in which the effective thickness of the coating in which the Lamb waves propagate is smaller than the measured thickness.

To quantify how the effective thickness of the coating changes when Cathode 1 is slightly calendered (from 48 µm to 45 µm), an illustrative model is shown in Fig. 5.7. The uncalendered battery film is a tri-layer structure consisting of a current collector, a coating and a mass loading layer. The mass loading layer provides a mass load on the effective coating layer, and Lamb waves do not propagates in the mass loading layer. By calendering the coating layer by a few micrometers, the rough surface flattens, and the pores are compressed. These changes result in increased effective coating thickness (h_{eff}) and reduced mass loading layer thickness. Since the sample has the lowest ZGV frequency when it is calendered to 45 µm as shown in Fig. 4.4, we assume that the mass loading layer disappears at that point. Since Lamb waves do not propagate in the mass loading layer, it is reasonable to simulate dispersion curves using a bilayer structure with higher density of the effective coating layer due to the mass loading effect, while considering the Young's modulus of the effective coating layer constant during this process. The density of the effective coating layer is estimated using Eq. 5.1, with $h = h_{eff}$. The Young's modulus of the effective coating layer is estimated at 0.39 GPa when the sample is calendered to 45 µm. Based on this estimation, the simulations indicates that the effective thickness is 18.3 µm for Cathode 1 (uncal) at 48 µm, and 35.9 µm when the sample is calendered to 47 µm.

Two simulated models with constant Young's modulus assumed for the coating are shown in Fig 4.4. The lowest ZGV frequency of the sample with thickness at 45 µm is used to estimate the Young's modulus value of the coating ($E = 0.39$ GPa). The density ρ of the coating is calculated according to h using Eq. 5.1. The corresponding M3-ZGV and M4-ZGV frequencies versus changes in thickness are then plotted. Similarly, the M4-ZGV frequency versus thickness is also plotted with an estimated $E = 3.4$ GPa for the coating.

By comparing the simulated models with the experimental results in Fig. 4.4, it is evident that the Young's modulus of the coating changes significantly during the calendering process. The ZGV measurement can be used to effectively monitor these changes. In Fig. 5.8, the estimated Young's modulus of the coating during the calendering process is shown. Error bars are estimated using a 95% confidence interval. Data is only presented for coating thicknesses less than 45 µm.

In Fig. 5.9, the sensitivity of the ZGV frequency to the changes in Young's modulus of the coating is calculated during the calendering process. The sensitivity (S) is calculated using $S = E/f_{ZGV}$ where E is the estimated Young's modulus from Fig. 5.8 and f_{ZGV} is the experimental ZGV frequency from Fig. 4.4. It can be observed that f_{ZGV} becomes more sensitive to small changes in E when the coating is calendered thinner, which makes the ZGV measurements more sensitive to changes in calendered films rather than uncalendered films.

In Fig. 4.4 it is evident that even though Cathode 1 (uncal) is calendered into same thickness (26µm) as the industrially calendered Cathode 1, the ZGV frequencies of these two battery films are significantly different. In the industry process, the battery film is calendered soon after the coating layer has dried [50] which appears to be capable of calendering the coating layer tighter, causing higher elasticity. In our work, the film was dried for a long time before the calendering process occurred. By comparing the SEM of Cathode 1 shown in Fig. 5.6 and the SEM of Cathode 1 (uncal) which was calendered to the same thickness, as shown in Fig. 5.5, the coating of the commercially calendered film appears to be more condensed than the film calendered in the laboratory, with generally smaller pores. The high compactness of the commercially calendered film would appear to have a higher Young's modulus and, therefore, higher ZGV frequency.

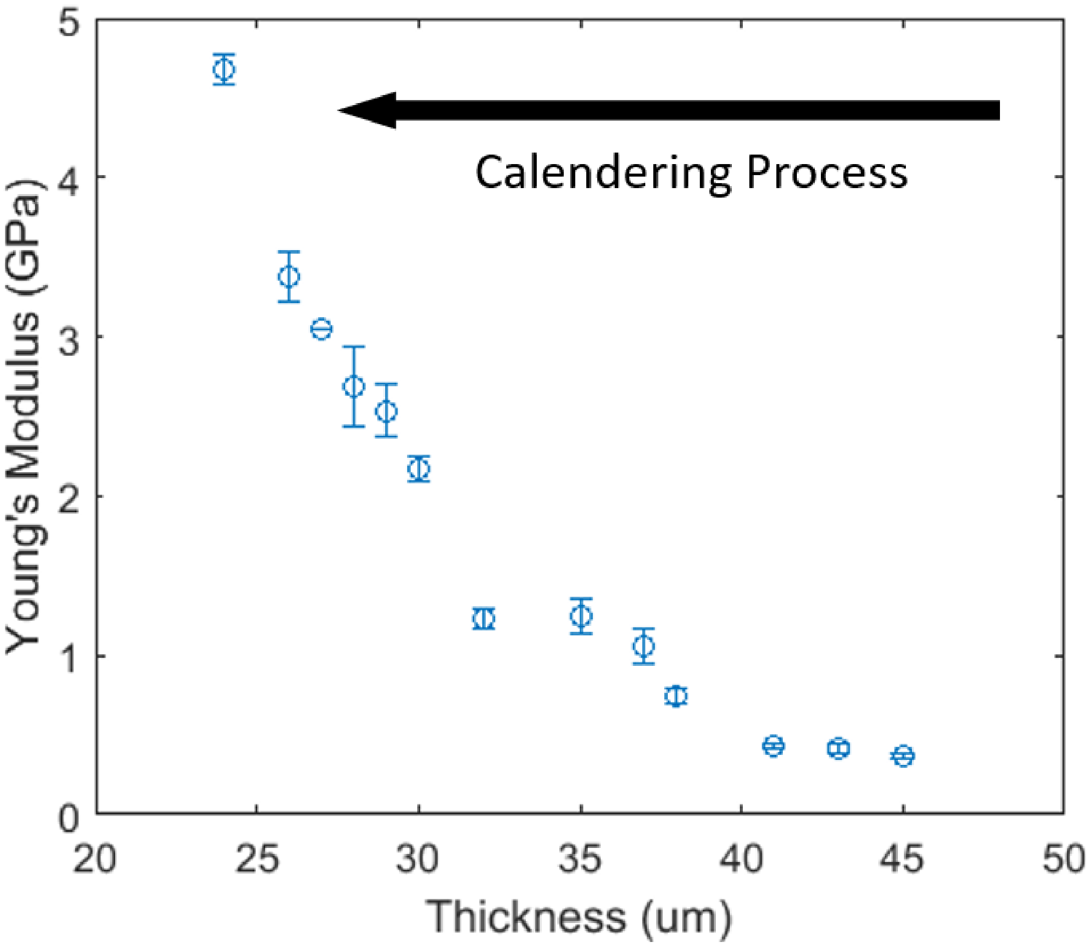

Figure 5.8: Young's modulus versus thickness of the coating of Cathode 1 (uncal) during the calendering process.

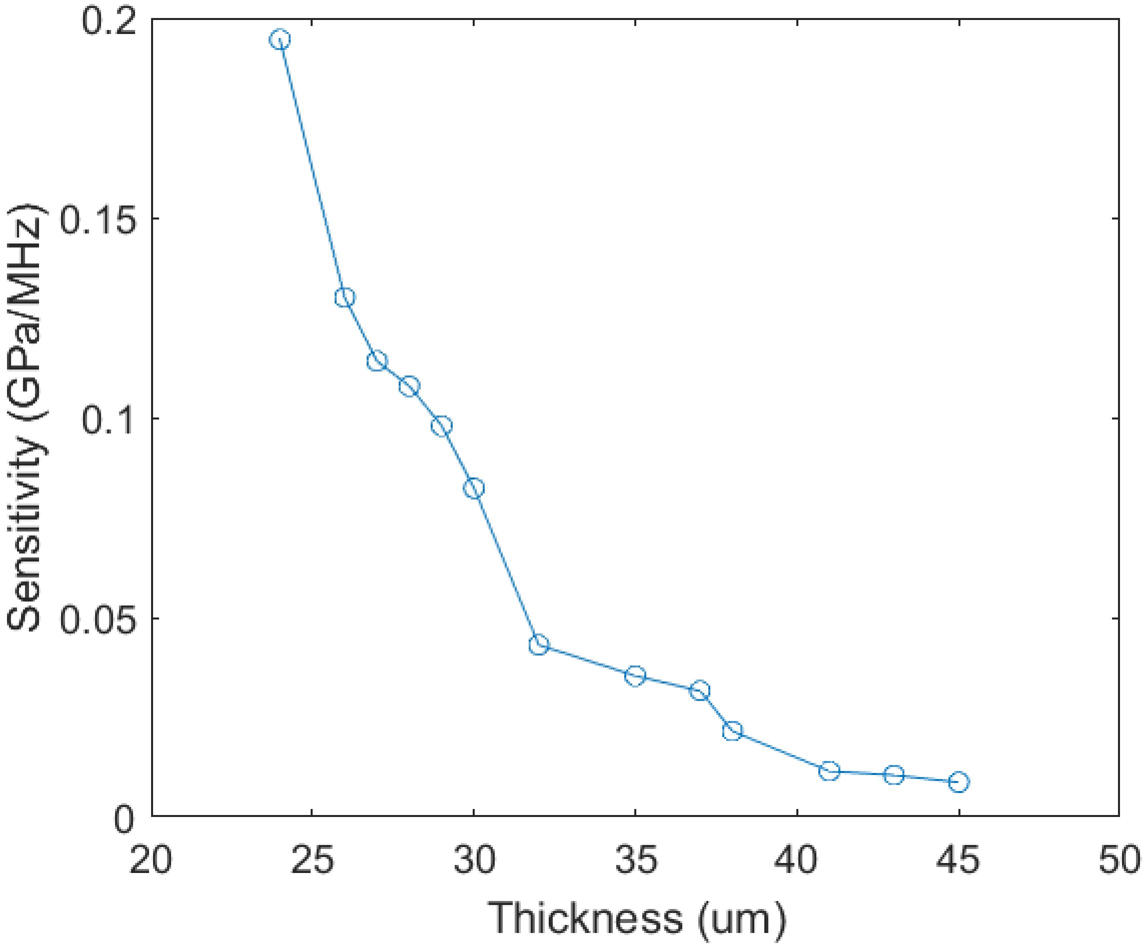

Figure 5.9: The sensitivity of ZGV frequency to Young's modulus of the coating of Cathode 1 (uncal) during the calendering process.

CHAPTER 6. CONCLUSION

6.1 Summary

In this thesis, different battery films with different mechanical properties are characterized using ZGV Lamb modes measurement. The Lamb waves of a bilayer structure consisting of a "compliant" layer and metallic layer are analyzed using dispersion curves. The theoretical model shows that ZGV Lamb modes exists for the battery films. Simulations done by using GUIGUW 2.2 software show that, when there is a huge difference between the elasticities of the two layers, both M3-ZGV and M4-ZGV can exist. The simulations shows that M3-ZGV mode have higher detectability than M4-ZGV mode. The ZGV modes are excited using a pulse laser and detected using a homo-dyne interferometer. As predicted by the simulations, cathodes and anode were distinguished between films with different mechanical properties. Mechanical properties change during the calendering process were monitored using ZGV measurements. The results shows that the Young's modulus of the battery coating changes significantly during the calendering process. The compression experiment further confirmed the Young's modulus difference between a calendered film and an uncalendered film.

6.2 Future Work

A lot more works need to be done in order to better understand the heterogeneity of battery films can be measured and controlled. Higher signal to noise ratio of the ZGV measurement can be achieved using a laser with higher power and more stable output. A stage with a precise motor can be used to scan the samples to generate maps of the distribution of different mechanical properties of battery films. It is possible to correlate ZGV Lamb mode with the porosity and roughness of the surface of battery coating by analyzing the combination of interferometric measurement scanning result and the SEM pictures of the scanned location.

Due to the non-destructive and non-contact properties of the propose measurement, this measurement can also be combined with the conductivity measurement on the same region of a battery film to determine if there is correlation between the electrical conductivity and mechanical properties to better study the electrode properties.

However, this method has its own challenge. The interferometeric measurement needs a reflective surface to form interference pattern. If the surface is not reflective enough or too rough, the interferometer cannot capture the ZGV Lamb mode because the low signal amplitude. Battery films are normally coated on both sides before its packaged, which means the interferometric measurement cannot be used since the battery coating is very dark. One way to solve this problem is using high power laser to ablate through the coating material until the metal electrodes are seen. As long as the wavelength of the ZGV modes are significantly longer than the radius of ablated coating material, the effect of ablation to ZGV Lamb waves is negligible. Even though this method is no longer non-destructive, it provides possibility to map out the distribution of coating material. Another way is to used surface acoustic wave detected by a high frequency transducer far away from the excitation point. But this method has to have contact with the battery electrodes and cannot locally measure the mechanical properties. In the mean time these transducers are also expensive to make.

Even though, compression method has been used to extract the Young's modulus value of different battery films, the result is very ambiguous and not accurate. Nanoindention method is needed to measure the Young's modulus of battery coating to further verify the extracted Young's modulus from the combination of ZGV modes and interferometric measurement.

The ultimate goal is to develop a probe that can be integrated into the roll-to-roll process to non-destructively quantify the heterogeneity of the mechanical properties of battery films. The heterogeneity of mechanical properties can then be correlated with the variations in electrical and ionic conductivity. A threshold is then needed to determine if the battery films are sufficiently homogeneous for packaging.

6.3 Conclusion

The interferometric ZGV measurement proposed in this work can quickly and accurately measure the mechanical properties of battery films. This work can also be generalized to measurements of other thin ”compliant”layer on thin layers of rigid material, providing a new tool for researchers investigating thin-film deposition. The sensitivities of ZGV modes to the change of mechanical properties of the coating layer were simulated. The mechanical properties such as ρ, E, h and ν of the battery coating affect acoustic bulk wave velocities that affect ZGV frequencies. Different commercial-graded battery films were characterized. With the combination of theoretical model and the interferometric measurements, the Young’s modulus of the battery coating layer was extracted, which is confirmed by alternative measurements. This non-contact and non-destructive evaluation technique can potentially be used to identify the heterogeneity of battery films to improve the safety and performance of batteries. As a potential control tool, it can reduce the scrap during manufacturing. The interferometric measurement can also be used to monitor the calendering process to track the elasticity of battery films before packaging.

REFERENCES

[1] M. M. A. Hussainb and A. Mohamedb, “A review of lithium-ion battery state of charge estimation and management system in electric vehicle applications: Challenges and recommendations,” *Renewable and Sustainable Energy Reviews*, vol. 78, pp. 834–854, 10 2017. 1

[2] N. Nitta, F. Wu, J. T. Lee, and G. Yushin, “Li-ion battery materials: present and future,” *Materials Today*, vol. 18, no. 5, pp. 252 – 264, 2015. [Online]. Available: http://www.sciencedirect.com/science/article/pii/S1369702114004118 1

[3] B. Scrosati and J. Garche, “Lithium batteries: Status, prospects and future,” *Journal of Power Sources*, vol. 195, no. 9, pp. 2419 – 2430, 2010. [Online]. Available: http://www.sciencedirect.com/science/article/pii/S0378775309020564 1

[4] J. Li, Z. Du, R. E. Ruther, S. J. AN, L. A. David, K. Hays, M. Wood, N. D. Phillip, Y. Sheng, C. Mao, S. Kalnaus, C. Daniel, and D. L. Wood, “Toward low-cost, high-energy density, and high-power density lithium-ion batteries,” *JOM*, vol. 69, no. 9, pp. 1484–1496, Sep 2017. [Online]. Available: https://doi.org/10.1007/s11837-017-2404-9 1

[5] G. Chen and T. Richardson, “Continuity and performance in composite electrodes,” *J. Power Sources*, vol. 195, no. 5387, 2010. 1

[6] S. J. Harris and P. Lu, “Effects of inhomogeneities nanoscale to mesoscale on the durability of li-ion batteries,” *J. Phys. Chem. C*, vol. 117, p. 6481, Feb 2013. 1, 2

[7] J. M. Tarascon and M. Armand, “Issues and challenges facing rechargeable lithium batteries,” *Nature*, vol. 414, pp. 359–367, November 2001. 2, 3, 4

[8] P. Bocchini, A. Marzani, and E. Viola, “Graphical user interface for guided acoustic waves,” *Journal of Computing in Civil Engineering*, vol. 25, no. 3, pp. 202–211, May 2011. 2, 11

[9] B. J. Lanterman, A. A. Riet, N. S. Gates, J. D. Flygare, A. D. Cutler, J. E. Vogel, D. R. Wheeler, and B. A. Mazzeo, “Micro-four-line probe to measure electronic conductivity and contact resistance of thin-film battery electrodes,” *Journal of The Electrochemical Society*, vol. 162, no. 10, pp. A2145–A2151, January 2015. 2, 4, 10

[10] K. L. Dallon, J. Yao, D. R. Wheeler, and B. A. Mazzeo, “Characterization of mechanical properties of battery electrode films from acoustic resonance measurements,” *Journal of Applied Physics*, vol. 123, no. 13, p. 135102, 2018. [Online]. Available: https://doi.org/10.1063/1.5021809 4, 6, 11, 40, 41

[11] J. E. Vogel, M. M. Forouzan, E. E. Hardy, S. T. Crawford, D. R. Wheeler, and B. A. Mazzeo, “Electrode microstructure controls localized electronic impedance in li-ion

batteries," *Electrochimica Acta*, vol. 297, pp. 820 – 825, 2019. [Online]. Available: http://www.sciencedirect.com/science/article/pii/S0013468618326884 4

[12] K. Zeng and J. Zhu, "Surface morphology, elastic modulus and hardness of thin film cathodes for li-ion rechargeable batteries," *Mechanics of Materials*, vol. 91, pp. 323 – 332, 2015, mechanics of energy conversion and storage. [Online]. Available: http://www.sciencedirect.com/science/article/pii/S0167663615001192 5

[13] S. S. Kumar, A. Fartash, M. Grimsditch, I. K. Schuller, and R. S. Kumar, "Elastic properties of polymer films. 1. elastic constants of a polyimide film determined by brillouin scattering and mechanical techniques," *Macromolecules*, vol. 26, no. 23, pp. 6184–6189, 1993. [Online]. Available: https://doi.org/10.1021/ma00075a008 5

[14] S. E. Bobbin, J. W. Wagner, and R. C. Cammarata, "Determination of the flexural modulus of thin films from measurement of the first arrival of the symmetric lamb wave," *Applied Physics Letters*, vol. 59, no. 13, pp. 1544–1546, 1991. [Online]. Available: https://doi.org/10.1063/1.106277 5, 6

[15] M. Castaings and P. Cawley, "The generation, propagation, and detection of lamb waves in plates using aircoupled ultrasonic transducers," *The Journal of the Acoustical Society of America*, vol. 100, no. 5, pp. 3070–3077, 1996. [Online]. Available: https://doi.org/10.1121/1.417193 5, 6

[16] P. M. G. Chow and J. Wang, "Correlation between laser-induced surface acoustic waves and nanoindentation on elastic modulus measurement of a nanoporous zeolite thin film," *J. Exp Mech*, vol. 55, p. 647, 2015. 5

[17] M. Ces, D. Clorennec, D. Royer, and C. Prada, "Thin layer thickness measurements by zero group velocity lamb mode resonances," *Review of Scientific Instruments*, vol. 82, no. 11, p. 114902, 2011. [Online]. Available: https://doi.org/10.1063/1.3660182 6, 7, 22

[18] J. Sermeus, R. Sinha, K. Vanstreels, P. M. Vereecken, and C. Glorieux, "Determination of elastic properties of a mno2 coating by surface acoustic wave velocity dispersion analysis," *Journal of Applied Physics*, vol. 116, no. 2, p. 023503, 2014. [Online]. Available: https://doi.org/10.1063/1.4885427 6, 7

[19] J. L. Tassoulas and T. R. Akylas, "On wave modes with zero group velocity in an elastic layer," *Journal of Applied Mechanics*, vol. 51, no. 3, pp. 652–656, September 1984. 6

[20] D. Clorennec, C. Prada, D. Royer, and T. W. Murray, "Laser impulse generation and interferometer detection of zero group velocity lamb mode resonance," *Applied Physics Letters*, vol. 89, no. 2, p. 024101, 2006. [Online]. Available: https://doi.org/10.1063/1.2220010 7, 10, 12, 22, 38

[21] S. Mezil, F. Bruno, S. Raetz, J. Laurent, D. Royer, and C. Prada, "Investigation of interfacial stiffnesses of a tri-layer using zero-group velocity lamb modes," *The Journal of the Acoustical Society of America*, vol. 138, no. 5, pp. 3202–3209, 2015. [Online]. Available: https://doi.org/10.1121/1.4934958 7, 22

[22] C. S. Suh and C. P. Burger, "Thermoelastic modeling of laser-induced stress waves in plates," *Journal of Thermal Stresses*, vol. 21, no. 8, pp. 829–847, 1998. [Online]. Available: https://doi.org/10.1080/01495739808956179 7

[23] F. Bruno, J. Laurent, P. Jehanno, D. Royer, and C. Prada, "Laser beam shaping for enhanced zero-group velocity lamb modes generation," *The Journal of the Acoustical Society of America*, vol. 140, no. 4, pp. 2829–2838, 2016. [Online]. Available: https://doi.org/10.1121/1.4965291 7

[24] O. Tofeldt and N. Ryden, "Zero-group velocity modes in plates with continuous material variation through the thickness," *The Journal of the Acoustical Society of America*, vol. 141, no. 5, pp. 3302–3311, 2017. [Online]. Available: https://doi.org/10.1121/1.4983296 7, 14

[25] D. Schneider and M. Tucker, "Non-destructive characterization and evaluation of thin films by laser-induced ultrasonic surface waves," *Thin Solid Films*, vol. 290-291, pp. 305 – 311, 1996, papers presented at the 23rd International Conference on Metallurgical Coatings and Thin Films. [Online]. Available: http://www.sciencedirect.com/science/article/pii/S0040609096090293 7

[26] A. Neubrand and P. Hess, "Laser generation and detection of surface acoustic waves: Elastic properties of surface layers," *Journal of Applied Physics*, vol. 71, no. 1, pp. 227–238, 1992. [Online]. Available: https://doi.org/10.1063/1.350747 7

[27] D. Hurley, V. Tewary, and A. Richards, "Thin-film elastic-property measurements with laser-ultrasonic saw spectrometry," *Thin Solid Films*, vol. 398-399, pp. 326 – 330, 2001, proceedings of the 28th International Conference on Metallurgic Coatings and Thin Films. [Online]. Available: http://www.sciencedirect.com/science/article/pii/S0040609001013384 7

[28] Q. Zhang, X. Xiao, Y. T. Cheng, and M. W. Verbrugge, "A non-destructive method for measuring the mechanical properties of ultrathin films prepared by atomic layer deposition," *Applied Physics Letters*, vol. 105, no. 6, p. 061901, 2014. [Online]. Available: https://doi.org/10.1063/1.4892539 7

[29] T. Grabec, P. Sedlk, P. Stoklasov, M. Thomasov, D. Shilo, M. Kabla, H. Seiner, and M. Landa, "In situ characterization of local elastic properties of thin shape memory films by surface acoustic waves," *Smart Materials and Structures*, vol. 25, no. 12, p. 127002, 2016. [Online]. Available: http://stacks.iop.org/0964-1726/25/i=12/a=127002 7

[30] S. Kitazawa, A. Chiba, and E. Wakai, "Laser-induced surface acoustic waves and their detection via diagnostic systems for detecting radiation damage on steel materials of nuclear devices," *Nuclear Instruments and Methods in Physics Research Section A: Accelerators, Spectrometers, Detectors and Associated Equipment*, vol. 786, pp. 47 – 50, 2015. [Online]. Available: http://www.sciencedirect.com/science/article/pii/S0168900215003599 7

[31] R. Cote, T. V. der Donck, J. Celis, and C. Glorieux, "Surface acoustic wave characterization of a thin, rough polymer film," *Thin Solid Films*, vol. 517, no. 8, pp. 2697 – 2701, 2009. [Online]. Available: http://www.sciencedirect.com/science/article/pii/S004060900801523X 7

[32] G. Chow, E. Uchaker, G. Cao, and J. Wang, "Laser-induced surface acoustic waves: An alternative method to nanoindentation for the mechanical characterization of porous nanostructured thin film electrode media," *Mechanics of Materials*, vol. 91, pp. 333 – 342, 2015, mechanics of energy conversion and storage. [Online]. Available: http://www.sciencedirect.com/science/article/pii/S0167663615002148 7

[33] J. Sermeus, R. Sinha, K. Vanstreels, P. M. Vereecken, and C. Glorieux, "Determination of elastic properties of a mno2 coating by surface acoustic wave velocity dispersion analysis," *Journal of Applied Physics*, vol. 116, no. 2, p. 023503, 2014. [Online]. Available: https://doi.org/10.1063/1.4885427 10

[34] M. Lowe, "Matrix techniques for modeling ultrasonic waves in multilayered media," *IEEE Transactions on Ultrasonics, Ferroelectrics, and Frequency Control*, vol. 42, no. 4, pp. 525–542, July 1995. 10

[35] H. Lamb, "On the flexure of an elastic plate," *London Math.Soc.*, vol. s1-21, no. 1, November 1889. 10

[36] L. Rayleig, "On the free vibrations of an infinite plate of homogeneous isotropic elastic matter," *London Math.Soc*, vol. s1-20, no. 1, pp. 225–237, November 1888. 10

[37] F. Chen and P. D. Wilcox, "The effect of load on guided wave propagation," *Ultrasonics*, vol. 47, no. 1-4, pp. 111–122, December 2007. 11

[38] I. Bartoli, A. Marzani, F. L. di Scalea, and E. Viola, "Modeling wave propagation in damped waveguides of arbitrary cross-section," *Journal of Sound and Vibration*, vol. 295, no. 3-5, pp. 685–707, August 2006. 11

[39] L. E. Kinsler, A. R. Frey, A. B. Coppens, and J. V. Sanders, *Fundamentals of Acoustics*, 4th ed. Wiley-VCH, December December 1999, no. pp. 560. 11, 27

[40] M. Chinmulgund, R. Inturi, and J. Barnard, "Effect of ar gas pressure on growth, structure, and mechanical properties of sputtered ti, al, tial, and ti3al films," *Thin Solid Films*, vol. 270, no. 1, pp. 260 – 263, 1995, 22nd International Conference on Metallurgical Coatings and Thin Films. [Online]. Available: http://www.sciencedirect.com/science/article/pii/0040609095069909 12

[41] C. Comte and J. von Stebut, "Microprobe-type measurement of young's modulus and poisson coefficient by means of depth sensing indentation and acoustic microscopy," *Surface and Coatings Technology*, vol. 154, no. 1, pp. 42 – 48, 2002. [Online]. Available: http://www.sciencedirect.com/science/article/pii/S0257897201017066 12

[42] J. Dolbow and M. Gosz, "Effect of out-of-plane properties of a polyimide film on the stress fields in microelectronic structures," *Mechanics of Materials*, vol. 23, no. 4, pp. 311 – 321, 1996. [Online]. Available: http://www.sciencedirect.com/science/article/pii/016766369600021X 12

[43] L. Brillouin, *Wave propagation in periodic structures; electric filters and crystal lattices, by Leon Brillouin*, 1st ed. McGraw-Hill Book Company New York, London, 1946. 12

[44] A. Gibson, J. Popovics, and M. Asce, “Lamb wave basis for impact-echo method analysis,” *Journal of Engineering Mechanics-asce - J ENG MECH-ASCE*, vol. 131, 04 2005. 18

[45] J. E. Vogel, M. M. Forouzan, E. E. Hardy, S. T. Crawford, D. R. Wheeler, and B. A. Mazzeo, “Electrode microstructure controls localized electronic impedance in li-ion batteries,” *Electrochimica Acta*, vol. 297, pp. 820 – 825, 2019. [Online]. Available: http://www.sciencedirect.com/science/article/pii/S0013468618326884 40

[46] O. Balogun, T. W. Murray, and C. Prada, “Simulation and measurement of the optical excitation of the s1 zero group velocity lamb wave resonance in plates,” *Journal of Applied Physics*, vol. 102, no. 6, p. 064914, 2007. [Online]. Available: https://doi.org/10.1063/1.2784031 40

[47] M. M. Forouzan, C. W. Chao, D. Bustamante, B. A. Mazzeo, and D. R. Wheeler, “Experiment and simulation of the fabrication process of lithium-ion battery cathodes for determining microstructure and mechanical properties,” *Journal of Power Sources*, vol. 312, pp. 172 – 183, 2016. [Online]. Available: http://www.sciencedirect.com/science/article/pii/S0378775316301227 40

[48] S. P. Nadimpalli, V. A. Sethuraman, D. P. Abraham, A. F. Bower, and P. R. Guduru, “Stress evolution in lithium-ion composite electrodes during electrochemical cycling and resulting internal pressures on the cell casing,” *Journal of The Electrochemical Society*, vol. 162, no. 14, pp. A2656–A2663, 2015. [Online]. Available: http://jes.ecsdl.org/content/162/14/A2656.abstract 40

[49] J. Newman, “Optimization of porosity and thickness of a battery electrode by means of a reactionzone model,” *Journal of The Electrochemical Society*, vol. 142, no. 1, pp. 97–101, 1995. [Online]. Available: http://jes.ecsdl.org/content/142/1/97.abstract 42

[50] Y. Sheng, C. R. Fell, Y. K. Son, B. M. Metz, J. Jiang, and B. C. Church, “Effect of calendering on electrode wettability in lithium-ion batteries,” *Frontiers in Energy Research*, vol. 2, p. 56, 2014. [Online]. Available: https://www.frontiersin.org/article/10.3389/fenrg.2014.00056 42, 46